REPUBLIC OF TURKEY

MUGLA SITKI KOÇMAN UNIVERSITY

GRADUATE SCHOOL OF NATURAL AND APPLIED SCIENCE

DEPARTMENT OF METALLURGICAL AND MATERIALS ENGINEERING

FCC-BCC PHASE STABILITY AND MAGNETISM IN $Mn_{20}Fe_{20}Co_{20}Ni_{20}Cu_{(20-x)}Al_x$ AND $Mn_{20}Fe_{20}Co_{20}Ni_{20}Cu_{(20-x)}Ga_x$ HIGH ENTROPY ALLOYS

MASTER OF SCIENCE (M.Sc.)

YAŞAR ORBAY

JAN 2023

MUGLA

REPUBLIC OF TURKEY

MUGLA SITKI KOÇMAN UNIVERSITY

GRADUATE SCHOOL OF NATURAL AND APPLIED SCIENCE

DEPARTMENT OF METALLURGICAL AND MATERIALS ENGINEERING

FCC-BCC PHASE STABILITY AND MAGNETISM IN $Mn_{20}Fe_{20}Co_{20}Ni_{20}Cu_{(20-x)}Al_x$ AND $Mn_{20}Fe_{20}Co_{20}Ni_{20}Cu_{(20-x)}Ga_x$ HIGH ENTROPY ALLOYS

MASTER OF SCIENCE (M.Sc.)

YAŞAR ORBAY

JAN 2023

MUGLA

MUGLA SITKI KOÇMAN UNIVERSITY

Graduate School of Natural and Applied Sciences

APPROVAL OF THE THESIS

The thesis submitted by **YAŞAR ORBAY** with the title of "**FCC-BCC Phase Stability and Magnetism in $Mn_{20}Fe_{20}Co_{20}Ni_{20}Cu_{(20-x)}Al_x$ and $Mn_{20}Fe_{20}Co_{20}Ni_{20}Cu_{(20-x)}Ga_x$ High Entropy Alloys**" has been unanimously accepted by the jury members of the 9th of January to fulfill the requirements for the degree of Master of Science in the Department of Metallurgical and Materials Engineering.

THESIS JURY MEMBERS

Assist. Prof. Dr. Tolga Tavşanoğlu **(Head of Committee)** Signature:

Department of Metallurgical and Materials Engineering,
Muğla Sıtkı Koçman University, Muğla

Assoc. Prof. Dr. Aslı ÇAKIR **(Supervisor)** Signature:

Department of Metallurgical and Materials Engineering,
Muğla Sıtkı Koçman University, Muğla

Assoc. Prof. Dr. Mehmet Şeref SÖNMEZ **(Member)** Signature:

Department of Metallurgical and Materials Engineering,
İstanbul Technical University, İstanbul

APPROVAL OF HEAD OF THE DEPARTMENT

Assoc. Prof. Dr. Gülhan ÇAKMAK, Head of Department Signature:

Department of Metallurgical and Materials Engineering,
Muğla Sıtkı Koçman University, Muğla

Assoc. Prof. Dr. Aslı ÇAKIR, Supervisor Signature:

Department of Metallurgical and Materials Engineering,
Muğla Sıtkı Koçman University, Muğla

Date of Defense: 09/01/2023

Tez çalışmalarım sırasında elde ettiğim ve sunduğum tüm sonuç, doküman, bilgi ve belgelerin tarafımdan bizzat ve bu tez çalışması kapsamında elde edildiğini; akademik ve bilimsel etik kurallarına uygun olduğunu beyan ederim. Ayrıca, akademik ve bilimsel etik kuralları gereği bu tez çalışması sırasında elde edilmemiş başkalarına ait tüm orijinal bilgi ve sonuçlara atıf yapıldığını da beyan ederim.

(I hereby declare that all information and documents within the scope of this thesis has been obtained and presented by me personally in complies with the academic and scientific ethical rules. I also declare that, as required by academic rules and ethical conduct, I have fully cited and references all materials and results that are not original during this thesis work.)

Yaşar ORBAY

09/01/2023

ABSTRACT

FCC-BCC PHASE STABILITY AND MAGNETISM IN $Mn_{20}Fe_{20}Co_{20}Ni_{20}Cu_{(20-x)}Al_x$ AND $Mn_{20}Fe_{20}Co_{20}Ni_{20}Cu_{(20-x)}Ga_x$ HIGH ENTROPY ALLOYS

Yaşar ORBAY

Master of Science (M.Sc.)

Graduate School of Natural and Applied Sciences

Department of Metallurgy and Material Engineering

Supervisor: Assoc. Prof. Dr. Aslı ÇAKIR

Jan 2023, 68 pages

In this study, the structural and magnetic properties of $Mn_{20}Fe_{20}Co_{20}Ni_{20}Cu_{(20-x)}Al_x$ and $Mn_{20}Fe_{20}Co_{20}Ni_{20}Cu_{(20-x)}Ga_x$ (x = 0, 5, 10, 15, 20 at %) high entropy alloys (HEAs) were investigated. The alloys were produced in an arc melter by using high purity elemental materials. The effect of varying Al and Ga contents on the crystal structures were studied using X-ray diffraction (XRD). Determination of the chemical compositions were performed by energy dispersive x-ray analysis (EDX). Magnetic properties were investigated with a superconducting quantum interference device (SQUID) magnetometer, and the micro-hardness of alloys was investigated using a Vicker-hardness tester.

From the XRD results, the face-centered cubic (FCC) crystal structure was observed for x = 0 and 5 at% Al and x = 0, 5 and 10 at% Ga. In addition to the FCC phase, the body-centered cubic (BCC) structure is formed by further increasing the amount of Al and Ga. Moreover, the equimolar $Mn_{20}Fe_{20}Co_{20}Ni_{20}Al_{20}$ HEA forms as the ordered intermetallic B2 phase as seen by the appearance of super-structure peaks. Magnetization measurements revealed that FCC and BCC structures emerge with their own characteristic magnetic properties. While the FCC phase exhibits ferromagnetic and anti-ferromagnetic mixed magnetic interactions, the BCC structure comes along with its soft magnetic behavior with pure ferromagnetism. The saturation magnetization, coercive fields, Curie temperatures and average magnetic moment values of each alloy and phase were determined and evaluated for all Al and Ga. Additionally, the exchange bias effect was observed as a result of ferromagnetic and antiferromagnetic mixed magnetic interactions. It vanishes for high amounts of Al and Ga. The valence electron numbers and average magnetic moments were interpreted in view of the Slater-Pauling rule for the two HEA series. Micro-hardness results show that the formation of the BCC structure leads to a distinct increase in the hardness for both Al and Ga addition. We have also investigated the magnetocaloric properties of these HEAs. The field dependent entropy change was studied for x = 0 at%. The maximum entropy change was found as 0.96 $Jkg^{-1}K^{-1}$ around Curie temperature at 5 T magnetic field. The entropy change does not reduce to zero in the measured temperature range.

Keywords: High Entropy Alloy, Magnetism, Crystal Structure, Micro-hardness

ÖZET

$Mn_{20}Fe_{20}Co_{20}Ni_{20}Cu_{(20-x)}Al_x$ VE $Mn_{20}Fe_{20}Co_{20}Ni_{20}Cu_{(20-x)}Ga_x$ YÜKSEK ENTROPİ ALAŞIMLARINDA FCC-BCC FAZ GEÇİŞİ VE MANYETİZMA

Yaşar ORBAY

Yüksek Lisans Tezi

Fen Bilimleri Enstitüsü

Metalurji ve Malzeme Mühendisliği Anabilim Dalı

Danışman: Doç. Dr. Aslı ÇAKIR

Ocak 2023, 68 sayfa

Bu çalışmada, $Mn_{20}Fe_{20}Co_{20}Ni_{20}Cu_{(20-x)}Al_x$ ve $Mn_{20}Fe_{20}Co_{20}Ni_{20}Cu_{(20-x)}Ga_x$ (x = 0, 5, 10, 15, 20 at %) yüksek entropi alaşımlarının (HEAs) yapısal ve manyetik özellikleri incelenmiştir. Alaşımlar, yüksek saflıkta elementler kullanılarak bir ark ergitme yöntemi ile üretilmiştir. Değişen Al ve Ga içeriklerinin kristal yapılar üzerindeki etkisi X-ışınları difraktometresi (XRD) kullanılarak incelenmiştir. Kimyasal bileşimlerinin belirlenmesi enerji dağılımlı x-ışını analizi (EDX) ile gerçekleştirildi. Manyetik özellikler, süper iletken kuantum girişim cihazı (SQUID) manyetometresi ile incelendi ve alaşımların mikro sertliği Vickers-sertlik test cihazı kullanılarak araştırıldı.

XRD sonuçlarından, x = 0 ve 5 %Al ve x = 0, 5 ve 10 % Ga için yüzey merkezli kübik (FCC) kristal yapısı gözlendi. FCC fazına ek olarak, Al ve Ga miktarının daha da artmasıyla hacim merkezli kübik (BCC) yapısı oluşur. Ayrıca eşmolar $Mn_{20}Fe_{20}Co_{20}Ni_{20}Al_{20}$ HEA, süper yapı piklerinin ortaya çıkmasıyla düzenli intermetalik B2 fazı olarak oluşur. Manyetizasyon ölçümleri, FCC ve BCC yapılarının kendi karakteristik manyetik özellikleriyle oluştuğunu ortaya çıkarmıştır. FCC fazı, ferromanyetik ve anti-ferromanyetik karışık manyetik etkileşimler sergilerken, BCC yapısı saf ferromanyetizma ile yumuşak manyetik davranışı ile ortaya çıkmıştır. Tüm Al ve Ga örnekleri için doygunluk manyetizasyonu, zorlayıcı alanları, Curie sıcaklıkları ve her bir alaşımın ve fazın ortalama manyetik moment değerleri belirlenmiş ve değerlendirilmiştir. Ek olarak, ferromanyetik ve anti-ferromanyetik karışık manyetik etkileşimlerin bir sonucu olarak exchange bias etkisi gözlenmiştir. Yüksek miktardaki Al ve Ga alaşımlarında bu etki kaybolmuştur. Değerlik elektron sayıları ve ortalama manyetik momentler, her iki HEA serisi için Slater-Pauling kuralına göre yorumlanmıştır. Mikro sertlik sonuçları, BCC yapısının oluşumunun hem Al hem de Ga ilavesi için sertlikte belirgin bir artışa yol açtığını göstermektedir. Ayrıca bu HEA'ların manyetokalorik özellikleri de araştırıldı. Alan bağımlı entropi değişimi, x = 0 için incelenmiştir. 5 T manyetik alanda Curie sıcaklığı etrafında maksimum entropi değişimi 0.96 Jkg-1K-1 olarak bulunmuştur. Entropi değişimi, ölçülen sıcaklık aralığında sıfıra düşmemiştir

Anahtar Kelimeler: Yüksek Entropi Alaşımı, Manyetizma, Kristal Yapı, Mikro-sertlik

Dedicated to my Precious Daughter “Buğlem”
and to my Beloved Wife.

ACKNOWLEDGEMENT

First of all, I would sincerely like to special thanks to my supervisor Assoc. Prof. Dr. Aslı ÇAKIR, for her support, guidance, knowledge, experience and opportunities has provided throughout my graduate thesis.

I warmly thank to my valuable professor, Assist. Prof. Tolga TAVŞANOĞLU, who helped me to keep on track with his friendly advice and motivations, beyond his immense teachings.

I am heartily grateful to Prof. Dr. Mehmet ACET for his invaluable contribution to this thesis through his vast knowledge and experience.

I want to express my sincere thanks to my mother and father for their support and encouragement at every stage in the decisions I made throughout my life.

I am obliged my deepest gratitude to my precious daughter and wife, who encourage me with their presence and they are the source of my happiness and greatest motivations. I am glad to have them.

TABLE OF CONTENTS

LIST OF TABLES

LIST OF FIGURES

LIST OF SYMBOLS AND ABBREVATIONS

θ	Contact Angle, 0
μ	Magnetic Moment
ΔS_{conf}	Configurational Entropy Change
R	Universal Gas Constant
e/a	Valance Electron Concentration
Å	Angstrom
HEA	High Entropy Alloy
T_c	Curie Temperature
M_s	Saturation Magnetization
M_r	Remnant Magnetization
H_c	Coercive Field
FCC	Face Centered Cubic
BCC	Body Centered Cubic
K	Kelvin
XRD	X-ray Diffraction
EDX	Energy Dispersive X-Ray Spectroscopy
TEM	Transmission Electron Microscopy
SEM	Scanning Electron Microscopy
M(T)	Temperature Dependent Magnetization
M(H)	Field Dependent Magnetization
B_{ext}	External Magnetic Field
SQUID	Superconducting Quantum Interference Device
VEC	Valance Electron Concentration

EB	Exchange Bias
AF	Antiferromagnetic
FM	Ferromagnetic
FW	Field Warming
FC	Field Cooling
ZFC	Zero Field Cooling
MCE	Magnetocaloric Effect
HV	Hardness Vickers
T	Tesla
Oe	Oersted

1. INTRODUCTION

1.1. General Concept of High-Entropy Alloy

Alloys with advanced properties make an irreplaceable contribution to the development of technology. Since the Bronze Age, humans have been investigating different types of materials with various alloying elements to obtain desired property. Conventional alloys are typically composed with the addition of a relatively small amounts of secondary elements to the primary component selected according to the property requirements. Adding tin to copper to make bronze or adding carbon to iron to make steel are classical and the first examples of traditional alloying. This traditional alloy strategy has led to the development of the physical and mechanical properties of materials for many years. The majority of high-performance alloys currently in use are a product of this conventional method. On the other hand, with evolved industry and technology, the search for new metallic materials with superior performance has paved the way for the coming of novel approaches. In that context, Cantor and Yeh independently worked on alloys consisting of five or more elements in equimolar or near equimolar ratios, which was defined as a new alloying strategy. Unaware of Yeh's work, Cantor was the first to do pioneering work to draw attention to new approach in 1981 with his student. However, he published the first article on this subject in 2004 and he described his new materials as "multicomponent alloys". Cantor et al. prepared alloys that have equimolar 20 elements each ratio of 5 at.% Mn, Cr, Fe, Co, Ni, Cu, Ag, W, Mo, Nb, Al, Cd, Sn, Bi, Pb, Zn, Ge, Si, Sb and Mg, and 16 elements each ratio of 6,25 at.% Mn, Cr, Fe, Co, Ni, Cu, Ag, W, Mo, Nb, Al, Cd, Sn, Pb, Zn, and Mg produced by induction melting. Same results were found for both alloys, polycrystalline microstructure and mechanically brittle. While studying the aforementioned two alloys, they discovered predominantly a main FCC crystal structure, in particular, in the regions with high concentrations of Cr, Mn, Fe, Co, and Ni elements. Then, they designed an equimolar $Cr_{20}Mn_{20}Fe_{20}Co_{20}Ni_{20}$ alloy which

exhibits single FCC phase and a typical dendrite structure. The equiatomic FeCrMnNiCo alloy is known as the "Cantor alloys" (Cantor et al., 2004). Yeh, independently has referred to the same concept and he defined these new concept alloys as “High-Entropy Alloys” (Yeh et al., 2004).

The first definition of HEAs based on compositional specifications is that as a new concept solid solution alloying strategy HEAs include five or more major metallic elements in equal or near-equal atomic percentage (at%) between 5% and 35% (Yeh et al., 2004).

Another definition of HEAs is related to the concept of entropy. The utilization of high mixing entropy to promote the development of solid solution phase is the essence of this concept. When the mole fraction of elements approaches the equimolar ratio, the entropy of mixing reaches the highest value. The degrees of freedom in a system are comprised of the atomic vibrational configuration, magnetic moment configuration, and atomic arrangement configuration. These parameters represent the mixing entropy of the system in thermodynamic aspect (Srivatsan & Gupta, 2020, Yeh et al., 2013). The mixing entropy of a system increases with increasing number of elements (Pu et al., 2019). In Figure 1.1, as a general classification of the mixing entropy for an equiatomic system is given as a function of the number of components.

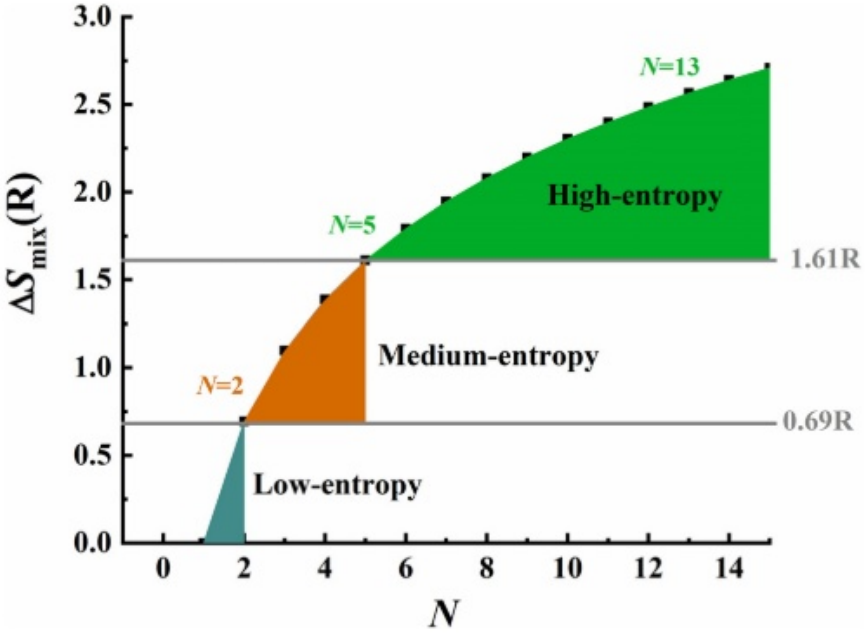

Figure 1.1 Mixing entropy of a system as a function of element number for equimolar alloys in totally disordered states (Pu *et al.*, 2019).

Yeh et al. defined the HEAs as an alloy with the configurational entropy ΔS_{conf} larger than 1.61R in their random solid solution state at room temperature, where R is the gas constant. This definition is expressed as,

$$\Delta S_{conf} \geq 1.61\, R \tag{1.1}$$

The formation of a solid solution from the mixing of "n" components results in configuration entropy, ΔS_{conf}, calculated by (Yeh et al., 2004),

$$\Delta S_{conf} = -R \sum_{i=1}^{n} x_i \ln x_i \tag{1.2}$$

Where R equals to 8.314 J/K mol., x_i is the molar fraction of i^{th} element and n is the total number of the components. The following equation is used to specify the configurational entropy change per mole, ΔS_{conf}, when n components of the system are in equimolar ratios at its liquid state or regular solid solution state (Yeh, 2006; Yeh et al., 2004).

$$\Delta S_{conf} = -R\left(\frac{1}{n}\ln\frac{1}{n} + \frac{1}{n}\ln\frac{1}{n} + \cdots \frac{1}{n}\ln\frac{1}{n}\right) = -R\ln\frac{1}{n} = R\ln n \tag{1.3}$$

ΔS_{conf} of HEAs is calculated according to Equation 1.3. The configurational entropy of the alloys with increasing number of constituent elements with equiatomic ratios is presented in Table 1.1.

Table 1.1 Configurational entropy of equiatomic alloys ($\Delta Sconf$) with constituent elements from 1 to 13 (Yeh, 2013)

n	1	2	3	4	5	6	7	8	9	10	11	12	13
ΔS_{conf}(R)	0	0.69	1.1	1.39	1.61	1.79	1.95	2.08	2.2	2.3	2.4	2.49	2.57

The configurational entropy of HEAs with five equimolar elements is calculated as 1.61R. Yeh et al. specified that multicomponent equiatomic alloys are classified into three categories as low-entropy alloys, medium-entropy alloys and high-entropy alloys (Yeh, 2006; Yeh, 2013) as shown in Figure 1.1. The alloys with configurational entropy less than 0.69R are known as low entropy alloys, while ΔS_{conf}(R) is in between 0.69R and 1.61R for medium entropy alloys, and higher than 1.61R for high entropy alloys.

1.2. Four Core Effects

In comparison to conventional alloys, HEAs have unique characteristics in terms of composition, kinetics, microstructure, and physical and mechanical properties. To identify the key characteristics of HEAs, Yeh et al. proposed four core effects: high-entropy effect for thermodynamics, sluggish diffusion effect for kinetics, severe lattice distortion effect for structure, and cocktail effect for properties (Yeh, 2006, 2013).

1.2.1. High entropy effect

Exhibiting a high configurational entropy is the main characteristic of HEAs. The solid solution formation from multi-principal-elements is mostly explained by the high-entropy effect. Instead of the formation of intermetallic phases, HEAs are mostly formed as BCC, FCC or HCP structures (Murty et al., 2019). In the conventional alloying strategy, the solid solution phases have also been found to have greater configurational entropy than that of intermetallic compounds (M. H. Tsai & Yeh, 2014). In thermodynamics, the Gibbs free energy change is given by $\Delta G = \Delta H - T\Delta S$ where ΔH is enthalpy change, T is temperature and ΔS is entropy change. High entropy change in a mixing means low Gibbs free energy change when the enthalpy change is assumed zero. HEAs with large number of components in equimolar or near-equimolar ratios will aid to maximize the configurational entropy change of mixing. The higher mixing entropy in HEAs reduces the Gibbs energy and promotes the formation of solid-solution phases instead of intermetallic compounds, particularly at high temperatures. High-entropy alloys crystallize mostly as a solid-solution creating a simple structure stabilized with the reduction of the Gibbs energy. In recent studies, it has been considered that it is not only the effect of mixing entropy but also the effect of mixing enthalpy and atom size difference that determines the phase formation of high entropy alloys (K. Zhang & Fu, 2012).

On the other hand, it is found that some HEAs may contain also intermetallic compounds in addition to the FCC and BCC phases especially after annealing at moderate temperatures although they are still above the limit of the high

configurational entropy value (Otto et al., 2013; M. H. Tsai & Yeh, 2014; K. Zhang & Fu, 2012).

1.2.2. Sluggish diffusion effect

When compared to conventional alloys, phase transformation kinetics and diffusion rates of atoms are slower in HEAs. The better high-temperature strength and structural stability and also formation of nanostructures and nano-sized precipitates have all been attributed to the sluggish diffusion effect due to the slow kinetics in HEAs (K. Y. Tsai et al., 2013).

In conventional alloying strategy, the local atomic configuration remains mostly the same after solute and solvent atoms jump and fill the vacancies. In HEAs, local atomic configuration is different before and after an atom diffuse into the vacancy, since every element with large portions has a different diffusion rate. Each region has a different local energy due to the differences in local atomic configuration. Each element has different melting temperatures, and the bond strengths are different, so some of them are more energetic. The more energetic atoms exhibit a very high affinity for atomic diffusion into the vacancies, and they are trapped when they jump into low-energy region. Nearest neighbor atomic diffusion becomes more difficult for the trapped atoms (M. H. Tsai & Yeh, 2014). Thus, the diffusion process is slowed down by this incident. The sluggish diffusion effect reduces the phase transformation rate in HEAs. This also influences the formation of the supersaturated state and nano-sized precipitates easily at high temperatures and additionally, contributes to obtain a high recrystallization temperature, slow grain growth, and excellent creep resistance (Murty et al., 2019).

1.2.3. Severe lattice distortion effect

The lattice of HEAs is highly distorted because of the different elements with different atomic sizes and different bonding energies. Therefore, the lattice distortion of HEAs is expected to be more severe compared to conventional alloys as seen in Figure 1.2 (Murty et al., 2019). Due to the severe lattice distortion, the properties of HEAs such

as hardness, strength, solid solution hardening, electrical resistance, and thermal resistance are affected severely (M. H. Tsai, 2013; Yeh, 2006).

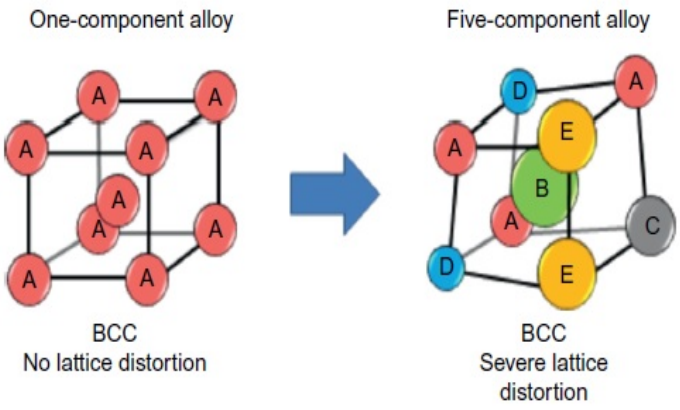

Figure 1.2 BCC lattice diagram showing lattice distortion comparison of conventional alloys and multicomponent alloys (Murty et al., 2019).

1.2.4. Cocktail effect

Ranganathan et al. was the first to propose that multi-metallic alloys have a cocktail effect, so multicomponent alloys were described by him as multi-material cocktails (Ranganathan, 2003). The characteristics of HEAs are strongly related to the characteristics of the constituent elements. While creating a HEA for a desired property, the inter-elemental interaction in the composing elements of mixing can give rise to observation of composite properties. Therefore, the inter-element factors should be considered before selecting elements when designing HEA. Indeed, the cocktail effect of multi-component mixing alloys has been encountered before the discovery of HEAs. Ti-Nb-Ta-Zr-O metallic glass alloys are designed by a car company and it is found that this alloy group exhibits a combination of remarkable properties like ultra-low elastic modulus and ultra-high strength in addition to Invar and Elinvar properties (Saito et al., 2003). Nowadays, this kind of multifunctionalities appear in different kinds of HEAs.

2. OVERVIEW

Recently, HEAs have attracted tremendous attention with excellent properties such as high strength (Senkov et al., 2014), high fatigue resistance (Hemphill et al., 2012), outstanding wear resistance (Chuang et al., 2011), high thermal stability (Wang et al., 2014), high fracture toughness (Gludovatz et al., 2014; Z. J. Zhang et al., 2015) and high electrical resistivity (Y. Zhang et al., 2013). All these properties makes HEAs attractive in many technological applications (M. H. Tsai & Yeh, 2014). Besides the mechanical properties, the physical features like magnetic and electrical transport properties of HEAs are also rather encouraging.

Initially, most of the studies have concentrated on the microstructures and mechanical characteristics of HEAs, whereas physical features such as magnetization and electric resistance have received less attention (M. H. Tsai, 2013). The magnetic properties of HEAs mainly depend on the alloying element and especially on the compositional diversity of magnetic elements found in HEAs (Mishra & Shahi, 2018).

Iron, cobalt, and nickel are ferromagnetic 3d-metals widely utilized in alloy production. The equiatomic CoCrFeNiCuAl alloy show impressive soft magnetic properties, like greater saturation magnetization (M_s) 38.18 emu/g and a lower coercive field (H_c) 16.08 emu/g due to its homogeneous polycrystalline microstructure compared with magnetic characteristic of bulk metals (Y. Zhang et al., 2014).

In terms of the mechanical properties, the $Al_xCoCrCuFeNi$ HEA system was studied by Tong et al. with changing Al content (Tong et al., 2005). Al is lightweight, soft and has a low melting point. They found that the alloy's micro-hardness and strength were increased considerably with increasing Al concentration, as shown in Figure 1.3. They reported that the formation of the BCC phase is promoted by the addition of Al. In addition to the strong bonding forces between Al and other elements, solid solution strengthening of Al atoms and the larger atomic radius of Al than the other atoms are responsible for the increase of hardness with increasing Al content.

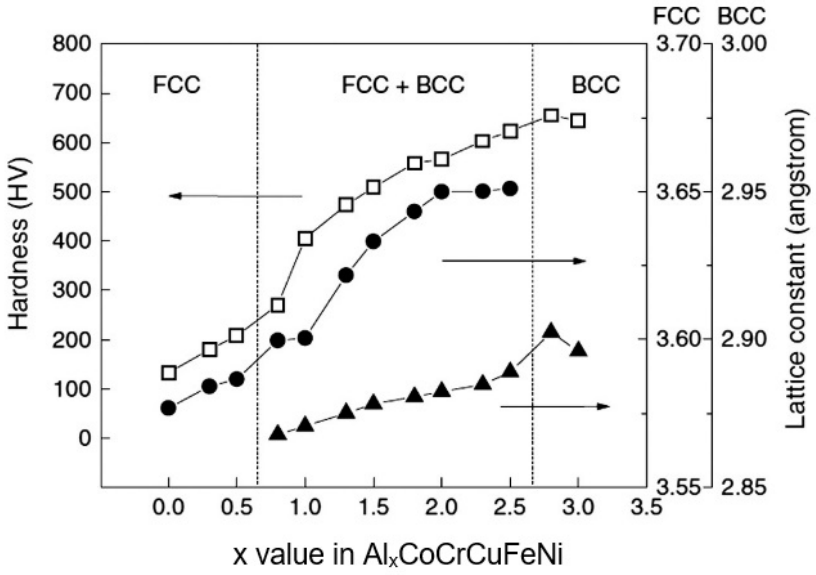

Figure 1.1 Effect of aluminum addition (x values) on the phase transformation of $Al_xCoCrCuFeNi$ high-entropy alloy, □ refers to hardness, ● refers to fcc phase, and ▲refers to bcc phase (Yeh, 2006).

Independently, Zhang et al., studied the effects of Al and Cu alloying on magnetic and mechanical properties of $FeCoNi(CuAl)_x$ (x=0-1.2, mol%) HEAs. It is observed that the crystallographic structures transform from FCC to BCC with increasing amount of Cu and Al which are diamagnetic and paramagnetic elements, respectively. They reported that a single FCC phase was present in the range $0 \leq x \leq 0.6$ and FCC/BCC duplex phases were obtained for $0.7 \leq x < 0.9$. For $0.9 \leq x \leq 1.2$, $FeCoNi(CuAl)_x$ HEA alloy was found to exhibit the BCC phase and minor FCC phase. They found the M_s of $FeCoNi(CuAl)_x$ HEAs decreased linearly, with increasing Cu and Al concentration. Also, they investigated the effect of annealing on the magnetic behavior of $FeCoNi(CuAl)_x$ HEAs. After annealing between 573-673 K, an increase in M_s from 78.9 Am^2/kg to 93.1 Am^2/kg was observed in the range of $0.7 \leq x < 0.9$, where only the BCC and FCC duplex phases were present. However, no changes were observed in M_s for other concentrations. They emphasized that the annealing of HEAs could be a potential method for obtaining high saturation magnetization and superior soft magnetic metallic alloys (Q. Zhang et al., 2016).

Additionally, Lucas et al. found that the alloy CoCrFeNi is a poor candidate for soft magnetic applications at high temperatures due to its low M_s and Curie temperatures

(T_c). They observed that the addition of Pd increases M_s and T_c. These alloys can be utilized for magnetic refrigeration applications by controlling T_c with Pd additions (Lucas et al., 2011).

Zhang et al. studied M_s, H_c and electrical resistivity (ρ) of the ternary FeCoNi alloy. After some addition of Al and Si, the electrical resistivity of $FeCoNi(AlSi)_x$ alloy dramatically increased from 16.7 μΩ-cm to 250 μΩ-cm by changing x up to 0,8. On the other hand, as the x value increased, a slight decrease was observed in saturation magnetization. (Y. Zhang et al., 2013).

Li et al. investigated the effect of Mn and Al contents on the magnetic and other physical properties of $FeCoNi(MnAl)_x$ high entropy alloys. They synthesized $FeCoNi(MnAl)_x$ alloys for x = 0, 0.5, 1, 1.5 and 2 by vacuum arc melting. It is reported that the alloys easily reach a high M_s with an applied magnetic field and show a low H_c when the applied magnetic field is removed or reversed indicating a soft-magnetic property. As given in Table 2.1, M_s values varies between 155.7 and 51.9 emu/g and the lowest value is found for $FeCoNiMn_{0.5}Al_{0.5}$ HEA.

On the basis of crystal structures, the addition of 3A and 4A elements into 3d element based HEA's, such as Al, Ga, Sn, leads to the partial formation of BCC structure (P. Li et al., 2017).

Zuo et al. investigated magnetic behaviors of CoFeMnNiX (X = Al, Cr, Ga, and Sn) high entropy alloys. They found that CoFeMnNi and CoFeMnNiCr alloys exhibit a simple FCC structure, CoFeMnNiAl alloy possesses an ordered BCC structure and CoFeMnNiGa alloy exhibits both FCC and BCC phases, but the BCC is much higher than the FCC phase given by the volume fraction. Therefore, structural change from FCC to BCC occurs by adding Al and Ga elements. They also reported the M_s and H_c values of these alloys determined from their hysteresis loops. The ferromagnetic properties of CoFeMnNiAl, CoFeMnNiGa, and CoFeMnNiSn alloys have been revealed by these M-H loops. In contrast, M-H of CoFeMnNiCr exhibits paramagnetic behavior. The obtained M_s and H_c values are collected in Table1.1. While M_s of CoFeMnNi and H_c is 18.14 Am^2/kg and 119 A/m, respectively, after Sn, Ga and Al were added, M_s increased to 80.29 Am^2/kg, 80.43 Am^2/kg and 147.86 Am^2/kg respectively. The H_c value of CoFeMnNiGa and CoFeMnNiSn alloys were found as 915 A/m and 3431 A/m, respectively. The CoFeMnNiSn alloy remains out of the scope

for soft magnetic behaviour, due to the H_c value being higher than 1000 A/m. It can be considered that the addition of Al and Ga compensates the antiferromagnetic character of manganese (Mn) atoms in CoFeMnNi. Furthermore, Al and Ga addition promote the formation of BCC. So it can also be concluded that the increasing value of M_s is correlated with the formation of the BCC phase (Zuo et al., 2017).

Table 2.1 Crystal structure, saturated magnetization (M_s) and coercivity (H_c) values of $FeCoNi(MnAl)_x$ alloys (P. Li et al., 2017) **and CoFeMnNiX (X = Al, Cr, Ga, and Sn) alloys (Zuo et al., 2017).**

Alloys	Structure	M_s (emu/g or Am^2/kg)	H_c(A/m)
FeCoNi	FCC	155.7	189
$FeCoNiMn_{0.25}Al_{0.25}$	FCC	101.0	268
$FeCoNiMn_{0.5}Al_{0.5}$	FCC + Minor BCC	51.9	730
$FeCoNiMn_{0.75}Al_{0.75}$	BCC + Minor FCC	129.6	445
FeCoNiMnAl	BCC	132.2	266
CoFeMnNi	FCC	18.14	119
CoFeMnNiSn	-	80.29	3431
CoFeMnNiGa	BCC + Minor FCC	80.43	915
CoFeMnNiAl	BCC	147.86	629
CoFeMnNiCr	FCC	1.39	10804

A further example of the studies on magnetic properties of HEAs is performed by Na et al.. They investigated the magnetic behavior in equiatomic FeCoNiCrX (X = Al, Ga, Mn, and Sn) HEAs. It is reported that FeCoNiCrMn and FeCoNiCrSn alloys exhibit paramagnetic behavior. Both Mn and Sn elements changed neither the structure nor the magnetic properties of the base FeCoNiCr alloy. However, the addition of Al and Ga in FeCoNiCr base alloy changed the structure from FCC to a duplex phase of

FCC and BCC and the magnetic state from paramagnetic to ferromagnetic. In addition to this, the M_s value significantly increased with the addition of Ga and Al in the base alloy from 0.5 emu/g to 38 emu/g and 25 emu/g, respectively. They also showed that the increase in M_s is related to the formation of BCC in addition to FCC (Na et al., 2018).

Another study was performed on structural, magnetic, and mechanical properties of $FeCoNi(CuAl)_{0.8}Ga_x$ ($0 \leq x \leq 0.08$) HEAs. It is obtained that the addition of Ga promotes the formation of the BCC phase. The formation of the BCC phase would increase the M_s value, due to the magnetic properties associated with the phase constitution. With increasing Ga concentration from 0 to 0.08, the saturation magnetization value gradually increased from 78.6 to 82.8 Am^2/kg. Additionally, the formation of the BCC phase, which is formed by the addition of Ga, is the most important factor in increasing both strength and hardness. They reported that the strength of the $FeCoNi(CuAl)_{0.8}Ga_x$ alloy increased with increasing Ga ratio (Z. Li et al., 2018).

Xu et al. studied the effect of Ag, Cu, and Co addition on the magnetic properties of mechanically alloyed FeSiBAlNi HEAs. They pointed out that M_s of FeSiBAlNi HEA decreased with the addition of Ag, Cu, and Co (Xu et al., 2016).

High Entropy $Fe_xCo_{1-x}NiMnGa$ alloys were synthesized by arc melting method and the effect of Fe or Co addition to the microstructure, mechanical and magnetic properties was investigated by Zuo et al.. They found that M_s for CoNiMnGa, $Fe_{0.5}Co_{0.5}NiMnGa$, and FeNiMnGa alloys were 115.92 emu/g, 78.48 emu/g, and 37.79 emu/g at 300 K, respectively. As the temperature decreases to 5 K, the value of M_s increases to 124.73 emu/g, 92.24 emu/g, and 81.73 emu/g for CoNiMnGa, $Fe_{0.5}Co_{0.5}NiMnGa$, and FeNiMnGa alloys, respectively. On the other hand, the H_c of the three alloys is found to be virtually identical at 300 K, with values of 28.4 Oe, 27.4 Oe, and 27.9 Oe for FeNiMnGa, $Fe_{0.5}Co_{0.5}NiMnGa$, and CoNiMnGa, respectively. The H_c of the $Fe_{0.5}Co_{0.5}NiMnGa$ and CoNiMnGa alloys retains almost the same (26.6 Oe and 27.4 Oe, respectively) at 5 K. However, at 5 K the H_c value of the FeNiMnGa alloy decreased to 20.8 Oe compared with the H_c at 300 K. In this study, it was emphasized that these three alloys exhibited excellent soft magnetic properties (Zuo et al., 2018).

Magnetic behavior of as-cast $FeNiCoMnCu_x$ alloy was studied by Rao et al. They observed an increase of M_s with increasing Cu content. They recorded M_s values as 9, 16 and 25 Am^2/kg, when x is equal to 0, 0.5 and 1 for $FeNiCoMnCu_x$ respectively (Rao et al., 2020).

Wu et al., investigated the effect of Ce addition to the $FeCoNiCuAlCe_x$ ($0 \leq x \leq 0.09$) HEAs on the magnetic properties, corrosion resistance, and microstructure. They observed that the initial and maximum permeability, maximum flux density, remanence and H_c decrease with the formation of the BCC phase. On the other hand, the FCC phase improves the initial and maximum permeability. Increasing the Ce amount helped the formation of the BCC phase, but the content of FCC phase decreased. In this study, the magnetic characteristics of FeCoNiCuAl HEA were significantly affected by a small quantity of Ce addition. They reported that all alloys have shown good soft magnetic properties. The addition of Ce led to the FCC phase changing from ferromagnetic to non-ferromagnetic in the HEAs (Z. Wu et al., 2022).

Guo et al. studied the effect of valance electron concentration (VEC) on phase stability in HEAs. They have shown that the VEC can be used to estimate the phase stability of FCC and BCC phases in HEAs. They found that the FCC phase is formed at higher VEC (≥8), while BCC phase is formed at lower VEC (<6.87) and mixed FCC and BCC phases are formed in between 6.87>VEC<8.0 (Guo et al., 2011).

In this study, we performed a systematic study on FCC-BCC phase transition and its effect on magnetic and mechanical properties of $(MnFeCoNi)_{80}Cu_{(20-x)}Al_x$ and $(MnFeCoNi)_{80}Cu_{(20-x)}Ga_x$ (x = 0, 5, 10, 15, 20 at %) HEAs. It is known from literature that the HEAs composed of 3d-transition metals exhibit the FCC structure. The BCC structure forms as a result of introducing a 3-4A group elements like Al, Sn, Ga and Si. Here, we chose equiatomic MnFeCoNiCu HEA as reference material and added Al and Ga in place of Cu by keeping the MnFeCoNi part at a constant molar ratio. Hence, we obtained two HEA series in a broad VEC (e/a) range. The structural, magnetic, magnetocaloric and micro-hardness properties were investigated. The average magnetic moment values were calculated from obtained results and they are evaluated in terms of Slater-Pauling rule.

3. EXPERIMANTAL PROCEDURE

3.1. Sample Preparation

Two different series of $(MnFeCoNi)_{80}Cu_{(20-x)}Al_x$ and $(MnFeCoNi)_{80}Cu_{(20-x)}Ga_x$ (x = 0, 5, 10, 15, 20 at %) HEAs were produced by vacuum arc melting method. The typical schematic of arc melting method is shown in Figure 3.1. In this method, an electric arc is created between negative and positive electrodes. Here, the negative electrode is tungsten with a sharp pointed end and the positive electrode is the Cu crucible. A water-cooling system is used to protect system from overheating and the melting process is performed under argon atmosphere.

The high purity of elemental bulk Mn, Fe, Co, Ni, Cu, Al, and Ga materials were weighed in required portions. Each sample was prepared by calculating their atomic percentages to be 4 gram in total and was placed into a water-cooled copper crucible seen in Figure 3.2. The melting process and solidification were conducted such that the water-cooled copper crucible was under argon atmosphere. Then, the produced HEA was repetitively melted and solidified by turning four times in order to ensure that the components were thoroughly combined with each other in their liquid condition so that chemical homogeneity improved.

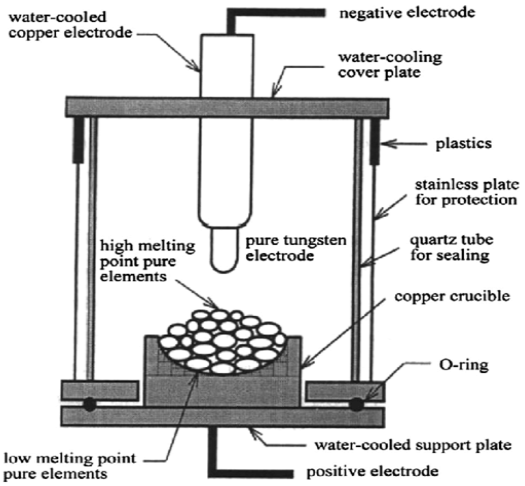

Figure 3.1 A schematic diagram of an arc melter (Chen et al., 2005)

The ingots were sealed in a quartz tube under argon atmosphere and kept at 1000 °C for 1 day for further homogenization. The samples were then quenched to room temperature in water.

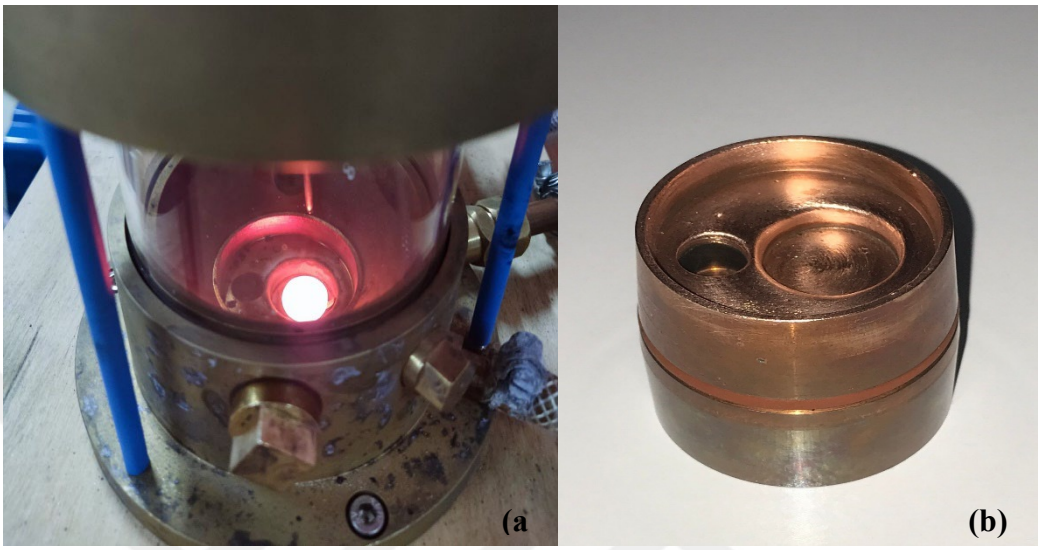

Figure 3.2 Images from the melting moment (a) and Cu crucible (b)

3.2. X-Ray Diffraction Measurements

X-ray diffraction (XRD) measurements were performed at room temperature with Bragg-Brentano focusing geometry and Cu-K_α radiation (λ-K_α=1.54 Å) over the range of $20° \leq 2\theta \leq 120°$ and the scanning rate was kept at 0,5°/min. The lattice parameters and crystal structures were obtained from the Rietveld refinement of X-ray data using Jana2006 software (Petricek et. al., 2014).

The XRD as one of the non-destructive testing methods is based on the principle that each crystal plane reflects X-rays in a different path depending on their unique atomic arrangement. These diffraction profiles for each crystal plane identify the crystal structure. The interaction of incident X-rays with the electrons of crystal atoms causes the scatter of incident X-rays. The interference of the reflected waves may be destructive or constructive when the incident plane wave hits the crystal at an arbitrary angle as an illustrated in Figure 3.3. Although these waves cancel each other out in

most directions due to destructive interference, they overlap in a few directions and form constructive interference, which is given by the Bragg law of scattering (Bragg et al., 1913):

$$2d \sin\theta = n\lambda \qquad (3.1)$$

Here d is the crystal spacing between diffracting planes, θ is the incident angle of x-rays relative to surface, λ is the beam wavelength, and n is the integer order of diffraction. According to Bragg's law, an x-ray diffractometer gives angle dependent intensity data indicating the crystalline planes of measured structures from a 2-5 μm depth from sample surface.

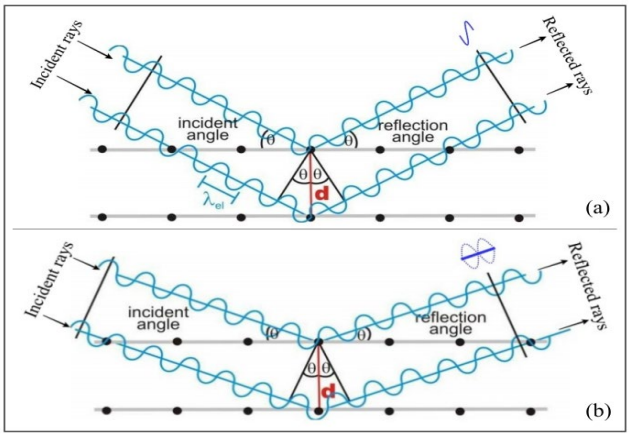

Figure 3.3 Bragg's law illustration. (a) Destructive interference, (b) Constructive Interference of reflected waves

3.3. Energy Dispersive X-ray Spectroscopy (EDX)

Energy dispersive X-ray (EDX) spectroscopy is performed to identify chemical quantities of elements in HEAs. The sample surfaces were polished for EDX mapping analysis by grinding with 320, 600, 800, 1200, 2000 and 4000 grid SiC abrasive paper.

EDX is an analytical technique performed by characteristic X-rays. It is used to ionize atoms in the sample and generally connected to a transmission electron microscopy (TEM) or scanning electron microscopy (SEM). As it is illustrated in Figure 3.4, secondary electrons with low energy are formed by the primary electron beam hitting an electron in an inner orbital and removes it from the orbital. Thus, the atom becomes

ionized and unstable. When another electron from the outer orbitals settles into the vacancy, the atom becomes stable again and the generated energy difference is emitted as x-rays such as K_α, L_α, M_α and K_β. Emitted X-rays are collected by the EDX detector. These characteristic x-rays are used to identify each element in the sample. By using a spectrum, histogram, and mapping, EDX can determine which elements are present and where they are located and how much they are in the sample.

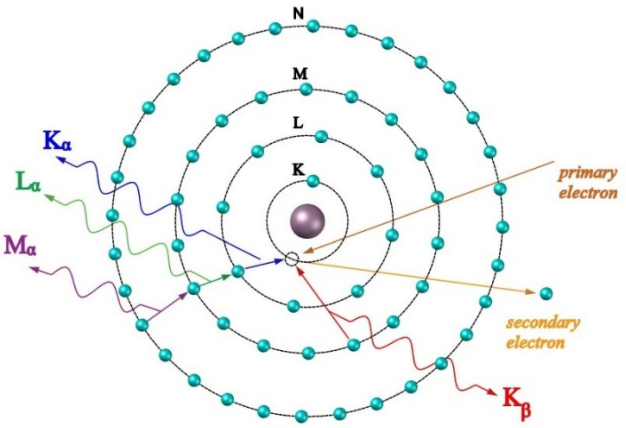

Figure 3.4 Schematic illustration of the EDX characterization.

3.4. Magnetization Measurements

Temperature-dependent magnetization M(T) measurements were performed under 5 mT and 5 T external magnetic fields in the temperature range of 10 K ≤ T ≤ 380 K and with an oven unit up to 780 K using Superconducting Quantum Interference Device (SQUID) magnetometer.

To determine the intrinsic magnetic behavior of the samples, low field (5 mT) measurements were performed. T_c were also obtained from these measurements. The M(T) measurements in the range 10 K ≤ T ≤ 380 K are performed in 3 stages which determine the magnetic and structural phase changes. These are zero-field-cooled (ZFC), field-cooled (FC), and field-warmed (FW) measurements. For ZFC measurement, first the sample was cooled down to 10 K from room temperature

without applying any external magnetic field. Then, a 5 mT magnetic field is applied and magnetization was measured by increasing the temperature from 10 K to 380 K The sample is magnetized spontaneously under the influence of an internal molecular interaction in ZFC condition. As a result, ZFC measurements shows how virgin magnetization varies with temperature. In the case of FC, the measurement was performed from 380 K to 10 K with an applied 5 mT magnetic field and magnetization was measured while cooling under the applied magnetic field. FW measurements were carried out at increasing temperatures from 10 K to 380 K with same external magnetic field. The M(T) measurements were also performed under 5T external magnetic field in order to obtain the saturation magnetization of alloys. Additionally, SQUID furnace was utilized for some samples for high temperature measurements.

In this study also, field-dependent magnetization M(H) measurements were performed using the SQUID magnetometer at 10 K for each alloy by applying a field in the range $-5\ T \leq B \leq 5\ T$. M(H) measurements generally are used to obtain H_c and the permeability of a ferromagnetic material.

3.5. Hardness Measurements

The resistance of a material to permanent deformation, such as indentation, abrasion, or scratch, is described as hardness. Hardness test is the most widely used mechanical test to determine the suitability of a material for a specific application and, to evaluate the properties of metals, in particular.

The microhardness values of the high entropy alloys produced in this study were measured using a Duroline M Micro Vickers Hardness Tester under 3N load with a dwell time of 10 seconds. At least 10 hardness measurements were taken from various regions of each alloy sample and the average was used as the micro-hardness value.

4. RESULTS AND DISCUSSION

In this section, the measurement results of $(MnFeCoNi)_{80}Cu_{(20-x)}Al_x$ and $(MnFeCoNi)_{80}Cu_{(20-x)}Ga_x$ with (x = 0, 5, 10, 15, 20 at %) HEAs will be given and discussed in two subsections with the order of XRD, EDX, magnetization and hardness. Additionally, magnetocaloric measurements for x = 0 alloy will be given as a third subsection.

4.1. $Mn_{20}Fe_{20}Co_{20}Ni_{20}Cu_{(20-x)}Al_x$ High Entropy Alloys

In this section, XRD, EDX, magnetization and hardness results of $(MnFeCoNi)_{80}Cu_{(20-x)}Al_x$ HEAs with x = 0, 5, 10, 15 and 20 at% will be given.

4.1.1. X-ray diffraction measurements

X-ray diffraction (XRD) patterns of each alloy are presented in Figure 4.1. The pure FCC crystal structure was detected for x = 0 and 5 at% alloys. Then, BCC crystal structure was formed in addition to FCC with increasing Al content. The evolution of BCC peaks is shown with arrows in Figure 4.1. The superstructure peaks of the BCC phase at 30° and 55° emerge for the alloy x = 20 at%. This means that a portion of BCC is ordered as B2 with the rest as Al. B2 is known as the ordered CsCl structure. Cl atoms take place at the body centers of cubic lattice and here, Al takes place at body centers in contrast to the randomly distributed other atoms.

To obtain the lattice parameters and the phase fractions of each phase, we performed Rietveld refinement of the XRD data. In the refinement results given in Figure.4.2a-d, the observed and calculated data are given in black and red lines, respectively. The blue lines represent the difference between observed and calculated data and vertical black lines correspond to the Bragg peak positions of FCC and BCC phases.

The refinements have been performed by profile fitting of the FCC structure with Fm-3m space group and a profile fitting of the BCC structure with Im-3m space group. For the alloy x = 20 at%, the fitting of the B2 structure (Figure.4.2d) was also

performed with Pm-3m space group and, it is observed that fitting B2 gives a better result than fitting BCC due to the presence of superstructure peaks at 30° and 55°. The formation of the B2 structure has also been detected in many kinds of HEAs which are mostly produced with 3d transition elements such as Fe, Co, Ni, Mn, Cu, Cr and Ti along with Al due to the strong affinity between Al and the other elements (Murty et al., 2019).

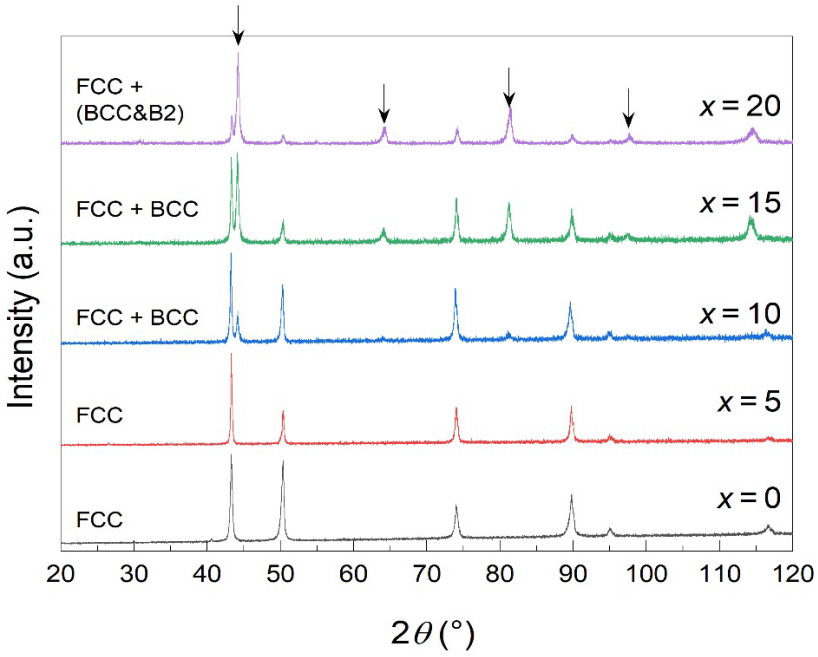

Figure 4.1 XRD data of $(MnFeCoNi)_{80}Cu_{(20-x)}Al_x$ HEAs.

The obtained lattice parameters and phase fractions of each phase are given in Table 4.1. The lattice parameter of the FCC structure first slightly increases with the addition of Al as a result of its larger atomic radius. Then, with the formation of the BCC phase, it decreases to its initial value for the alloy x = 15 at% and even below it for the alloy x = 20 at%. The lattice parameter of the BCC structure remains the same for the alloys x = 10 and 15 at%. Then, it decreases slightly for x = 20 at% alloy. This can be attributed to the formation of the ordered B2 structure. Al with large atomic radius replaces the body centers by letting the other atoms with relatively small radius to sit at the corners of cubic structure.

The phase fractions, also given in Table 4.1 show that the BCC phase is initially formed with 14% for the alloy x = 10 at%. The fractions of FCC and BCC are almost

equal for the alloy with x = 15 at%. Then, 23% of FCC occurs in the structure for the alloy x = 20 at% being the alloy with highest amount of Al. The rest of the alloy with 77% is composed of BCC/B2.

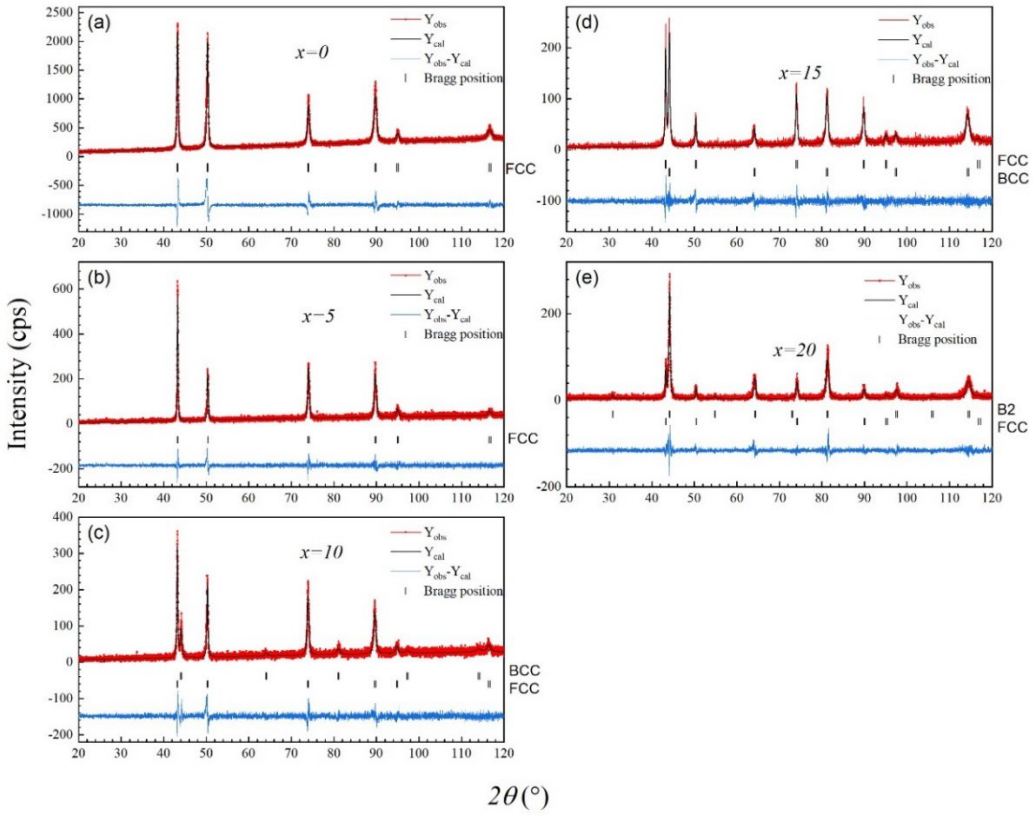

Figure 4.2 Rietveld refinement XRD data of $Mn_{20}Fe_{20}Co_{20}Ni_{20}Cu_{(20-x)}Al_x$ HEAs, (a) x=0, (b) x=5, (c) x=10, (d) x=15 and (e) x=20 obtained by Jana2006

Table 4.1 Lattice parameters and phase fractions of fcc and bcc phases for $(MnFeCoNi)_{80}Cu_{(20-x)}Al_x$ HEAs.

x (at%)	Lattice Parameters		Phase Fractions	
	fcc (Å)	bcc (Å)	fcc	bcc
x=0	3.6201	-	1	-
x=5	3.6239	-	1	-
x=10	3.6276	2.9022	0.86	0.14
x=15	3.6203	2.9020	0.45	0.55
x=20	3.6170	2.8991	0.23	0.77 **(BCC&B_2)**

4.1.2. EDX analysis

In order to determine the chemical composition of the phases and the element distributions of $(MnFeCoNi)_{80}Cu_{(20-x)}Al_x$ HEAs, EDX mapping and point analysis were performed. In the present study, after identifying the phase boarders by mapping, the nine random EDX spectra were obtained for each phase to obtain the average phase compositions. Figure 4.3 shows the electron image and the results of EDX-mapping for all elements. The scale bar given on the electron images corresponds to 50 μm in length. Table 4.2 shows the result of EDX point analysis and corresponding e/a values of the alloys.

According to mapping results given in Figure 4.3a-e, the alloys with x = 0 and 5 at% (Figure 4.3a-b) were formed with a homogeneous distribution of all elements which correlates with the existence of single FCC structure.

The first BCC phase was observed in x=10 at% (Figure 4.3c) HEA which contains two different regions in elemental mapping that are darker and brighter. The main phase of this alloy is the FCC structure with a larger phase fraction as seen in Table 4.1. It is understood that for Al and Ni, the darker areas represent the FCC phase and the brighter areas corresponds to the BCC phase. The completely opposite situation occurs for Fe. The darker regions represent the BCC phase, while the brighter regions correspond to the FCC phase. It can be clearly understood that the BCC phase is enriched with Al and Ni, while the FCC phase is enriched with Fe. A dendritic structure was observed at x=15 at% (Figure 4.3d) alloy because of solidification followed by arc melting. For this sample, the phase fractions of both FCC and BCC are almost equal to each other, so it is seen that the main matrix phase has changed to BCC and FCC structure formed as dendrites. For the sample x = 20 at% (Figure 4.3e), the main matrix of alloy becomes the BCC/B2. When we look for the elemental distribution for each phase, Co, Cu and Mn are almost similar in value of the atomic concentration for both FCC and BCC phases. We do not observe any distinct change in mapping for these elements. However, Fe, Ni and Al exhibit significant differences in compositions of the two phases. While most of the Fe prefers to remain in the FCC structure, Ni and Al prone to be in the BCC structure mostly.

Additionally, as shown in Figure 4.4a-b, EDX elemental mapping was also performed with a lower magnification for the x =20 at% alloy to interpret the grain structure in more detail. The scale bar in Figure 4.4b corresponds to 100 µm. At this magnification, it is clearly seen that the FCC phase occurs only at the grain boundaries as precipitates. This can also be associated with the formation of the ordered intermetallic B2 phase.

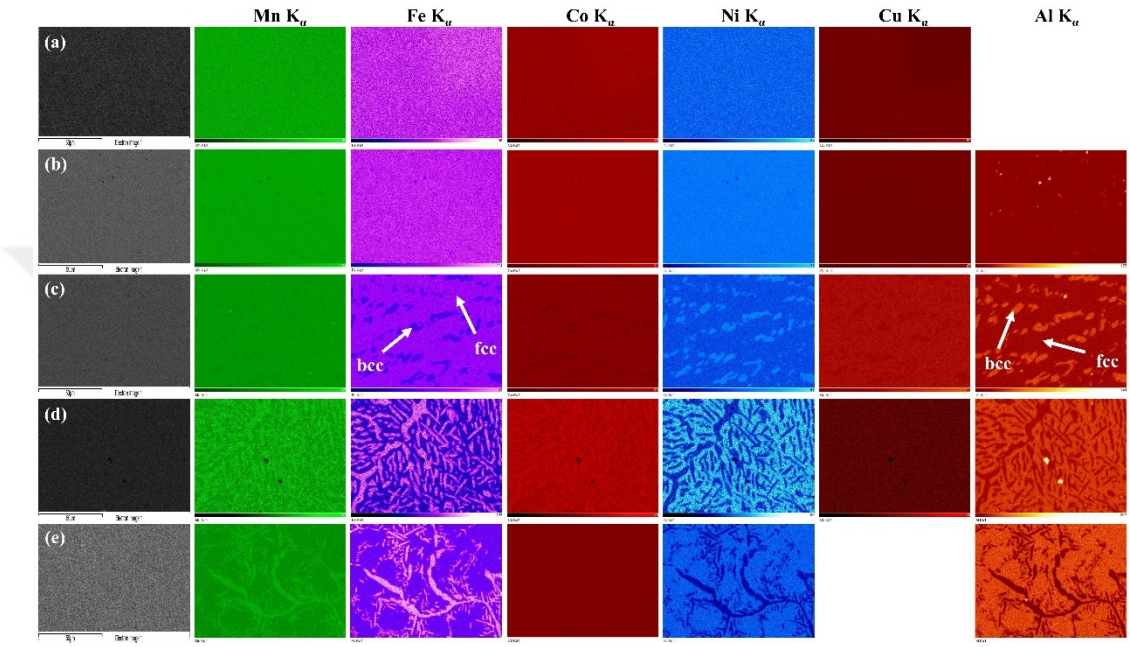

Figure 4.3 EDX elemental mapping analysis of $(MnFeCoNi)_{80}Cu_{(20-x)}Al_x$ HEAs, (a) x=0, (b) x=5, (c) x=10, (d) x=15 and (e) x=20 from the same region (50 µm magnification)

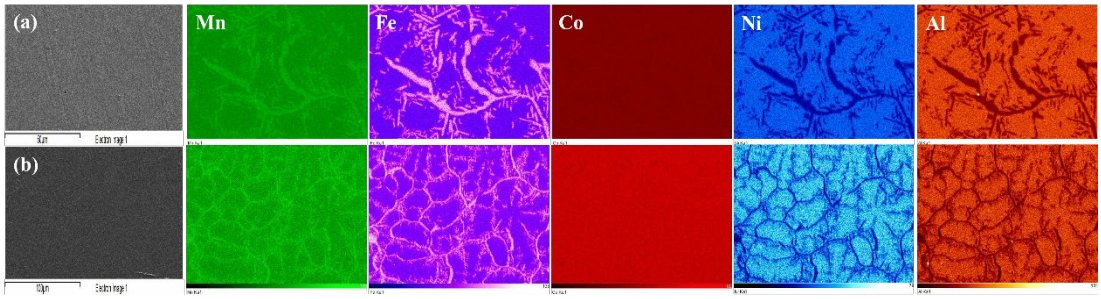

Figure 4.4 The comparison of $(MnFeCoNi)_{80}Al_{20}$ HEA at different areas and different scales a) 50µm magnification b) 100µm in given scale bar.

In Table 4.2, the compositions obtained from EDX analysis and corresponding e/a values are given. As a compositional comparison, x = 0 and 5 at% alloys exhibit a

homogeneous single-phase FCC structure. For x = 10, 15 and 20 at%, the sample exhibit both the FCC and BCC phases together. This means that Al addition facilitates the formation of the BCC phase with high amount of Al. From the compositions, it is clearly seen that Al and Ni are enriched in the BCC phase, while Fe is enriched in the FCC phase.

Table 4.2 Chemical compositions (at%) and e/a values of each sample for $(MnFeCoNi)_{80}Cu_{(20-x)}Al_x$ HEAs.

Al (at%)	FCC		BCC	
	Chemical Composition	**e/a**	**Chemical Composition**	**e/a**
x=0	$Mn_{18.2}Fe_{21.0}Co_{21.0}Ni_{20.5}Cu_{19.3}$	9.02	--	-
x=5	$Mn_{19.8}Fe_{20.6}Co_{20.7}Ni_{20.1}Cu_{14.0}Al_{4.8}$	8.73	--	-
x=10	$Mn_{19.3}Fe_{22.2}Co_{21.0}Ni_{19.7}Cu_{10.6}Al_{7.2}$	8.37	$Mn_{17.9}Fe_{13.8}Co_{17.8}Ni_{25.9}Cu_{8.4}Al_{16.2}$	7.96
x=15	$Mn_{20.7}Fe_{27.3}Co_{21.9}Ni_{16.3}Cu_{5.4}Al_{8.5}$	8.08	$Mn_{18.0}Fe_{15.5}Co_{19.1}Ni_{23.4}Cu_{5.0}Al_{19.1}$	7.68
x=20	$Mn_{24.2}Fe_{37.2}Co_{20.8}Ni_{11.3}Al_{6.5}$	7.87	$Mn_{17.8}Fe_{17.0}Co_{21.2}Ni_{23.2}Al_{20.9}$	7.46

The e/a values for each phase given in Table 4.2 span in a large range between $9.02 \geq e/a \geq 7.46$ including some critical values for physical properties of 3d-transition metals and elements. As an example, e/a = 8 corresponds to the value for FCC-Fe, the properties observed for FCC-Fe such as anti-Invar can also be observed in other 3d-metal alloys. $Fe_{64}Ni_{36}$ Invar alloy with e/a =8.7 exhibits a low coefficient of thermal expansion. This means that in this study, the alloy with x = 5 at%, having the same e/a value, can also exhibit low thermal expansion. It is observed that e/a values decrease with increasing the Al content, and the BCC phase gradually stabilizes accordingly. One of the main parameters to classify the phase formation in HEAs is e/a. It has been found in recent years that the stability of the FCC and BCC solid solution phases is strongly influenced by e/a (Guo et al., 2011). The FCC phase is stable for $e/a \geq 8$, and duplex BCC and FCC phases are formed for $6.87 < e/a < 8.0$.

4.1.3. Magnetization measurements

The magnetization measurements have been carried out as temperature-dependent M(T) and field-dependent M(H). M(T) measurements were carried out under 5 mT and 5 T external magnetic fields using a SQUID magnetometer in the temperature range of 10 K ≤ T ≤ 380 K. For some compositions such as x = 0, 10, 15 and 20 at%, magnetization measurements were also done at high temperatures in the range 380 K ≤ T ≤ 780 K under a 5 mT external magnetic field with an oven installed to the SQUID magnetometer.

The results of the measurements performed at 5 mT external magnetic field are given in Figure 4.5a-e. The temperature range of 10 K ≤ T ≤ 380 K is indicated with a blue line and the range of 380 K ≤ T ≤ 800 K is indicated with a red line. The low temperature M(T) measurements were carried out in ZFC, FC and FW sequences.

T_cs are obtained for each sample in these measurements. T_c is the temperature corresponding to the magnetic transition when a ferromagnetic material loses its permanent alignment and becomes paramagnetic at high temperatures. In Figure 4.5a-e, the point where the derivative of the magnetization with respect to temperature reaches a minimum gives T_c. In this context, T_c values were obtained by taking the derivatives of the M(T) measurements. For x = 0 at%, as given in Figure 4.5a, the alloy exhibits a paramagnetic (PM) behavior at high temperatures, then ferromagnetic (FM) ordering is observed below T_c = 378 K. The splitting between ZFC and FC measurements indicates that the material embodies both FM and anti-ferromagnetic (AF) mixed magnetic ordering together. This gives rise to a spin glass state as observed in the ZFC and FC measurements. During the ZFC process, the spins are frozen at a certain temperature which is called the freezing temperature (T_f) and they are no longer affected by the external magnetic field. This state is known as a spin glass magnetic state. So, splitting starts after this point. Such a splitting is often a sign of various configurational locking of remnant or intrinsic ferromagnetic components by the antiferromagnetic environment (Mañosa et al., 2003). A similar PM-FM transition with T_c = 220 K and ZFC-FC splitting are observed for the sample with x = 5 (Figure 4.5b). Adding a small amount of Al instead of Cu gives rise to a decrease in the magnetic ordering temperature. For the sample x = 10 (Figure 4.5c), in addition to T_c

of the FCC structure around 130 K, the second T_c at 745 K emerges with the formation of the BCC phase. For x = 15 (Figure 4.5d), the T_c of BCC phase shifts to a higher value around 770 K while the T_c of FCC almost vanishes. As given in the inset of Figure 4.5d, a small cusp at 80 K only remains, and this cusp is an indication for the AF ordering temperature, T_N. For this alloy, e/a = 8.08 for the FCC phase which is almost equal to that of metastable fcc γ-Fe with a T_N = 80 K. The magnetic ordering temperature related to the FCC phase vanishes for the alloy x = 20 at% and T_c of BCC/B2 structure is located at 735 K (Figure 4.5e). The decrease in T_c can be attributed to the formation of ordered B2 phase.

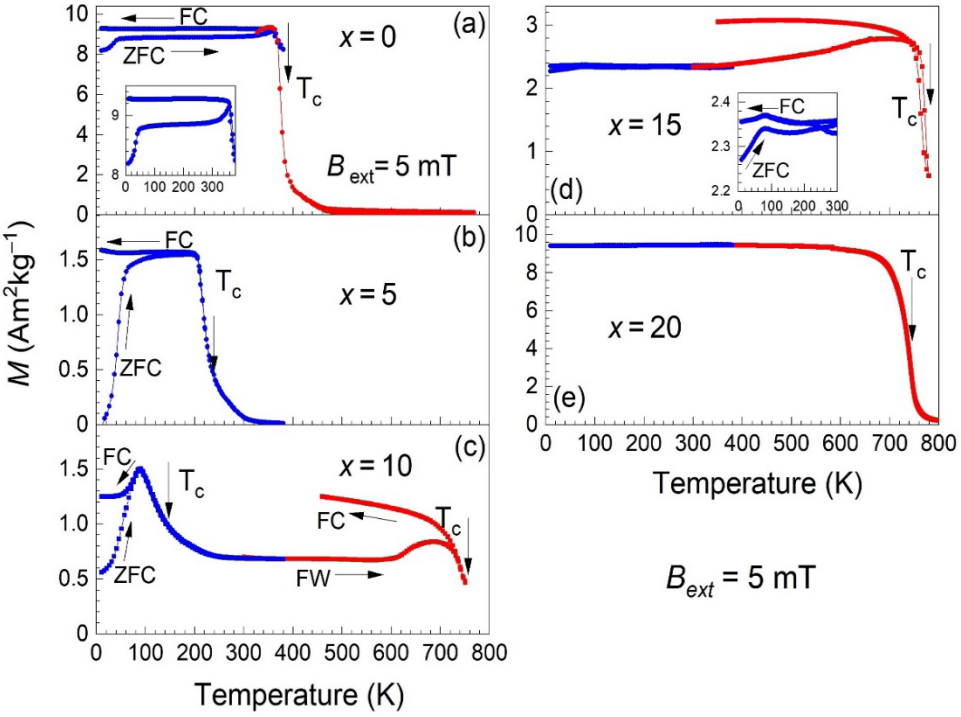

Figure 4.5. Temperature-dependent magnetization curves under 5 mT external magnetic field for $(MnFeCoNi)_{80}Cu_{(20-x)}Al_x$ with x = 0, 5, 10, 15 and 20 at% represented in (a), (b), (c), (d) and (e) respectively.

The results of the M(T) measurements performed under 5 T external magnetic field are given in Figure 4.6. The purpose of these measurements carried out under a high magnetic field is to find the saturation magnetization. The M_s and T_c values are collected in Table 4.3. M_s first decreases with increasing amount of Al and then increases with the formation of the BCC phase. The maximum M_s value was obtained

for the Cu-free alloy as 102 Am^2k^{-1}. It is clear that the formation of the BCC/B2 phases is the main factor for increasing M_s. This increase was also supported by some other researches performed on HEAs (P. Li et al., 2017; Z. Li et al., 2018; Na et al., 2018; Zuo et al., 2017).

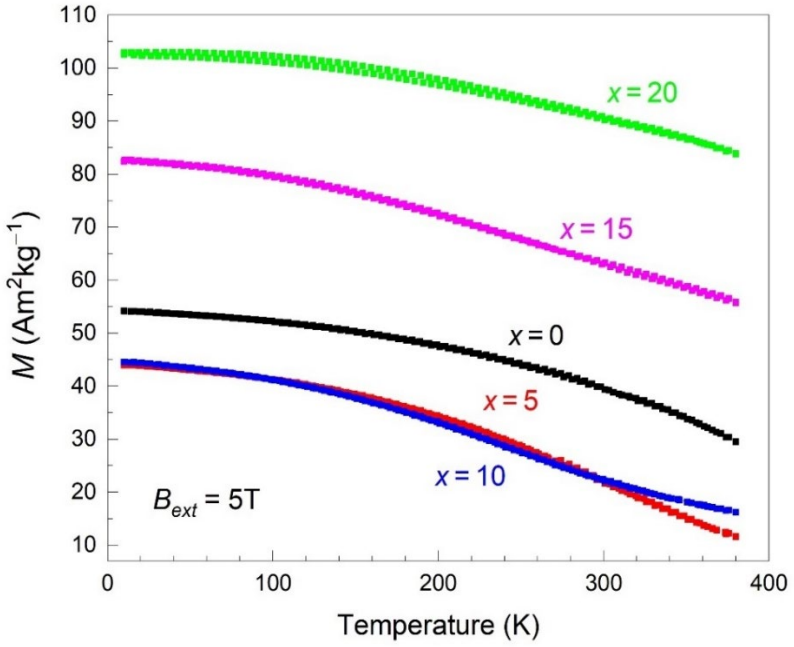

Figure 4.6 Magnetization measurements as a function of temperature $(MnFeCoNi)_{80}Cu_{(20-x)}Al_x$ HEAs obtained from a magnetic field of 5 T.

Table 4.3 Saturation magnetization (M_s), curie temperature (T_c) of $(MnFeCoNi)_{80}Cu_{(20-x)}Al_x$ HEAs.

Al (at%)	M_s (Am^2/kg)	T_c(K)	
		FCC	BCC
x=0	54	378	-
x=5	43	220	-
x=10	45	130	745
x=15	82	80 (T_N)	770
x=20	102	-	735

M(H) measurements of the $(MnFeCoNi)_{80}Cu_{(20-x)}Al_x$ alloys are shown in Figure 4.7. The parameters obtained from magnetization measurements such as M_s and coercive field (H_c) are shown as a function of Al content and are given in Figure 4.8.

The magnetic hysteresis loops of all these alloys resemble typical ferromagnetic and soft magnetic materials behavior. The loops in soft magnetic materials are quite narrow and they show low H_c (Coey, 2010). The H_c of these samples firstly increases for x = 0, 5 and 10, then a significant drop occurs for x = 10 and 20 alloys. The values of H_c for the synthesized HEAs are found to be 360 Oe, 930 Oe, 1120 Oe, 40 Oe and 7 Oe. The low H_c and high M_s values are associated with the presence of the pure ferromagnetic interactions for x = 20 alloy. The formation of the BCC/B2 phase with increasing Al content is directly related to the increase of M_s and the decrease of H_c. We can therefore conclude that these alloys exhibit soft magnetic behavior for high Al contents, and FM-AF mixed magnetic interactions are observed for the alloys with low Al amount.

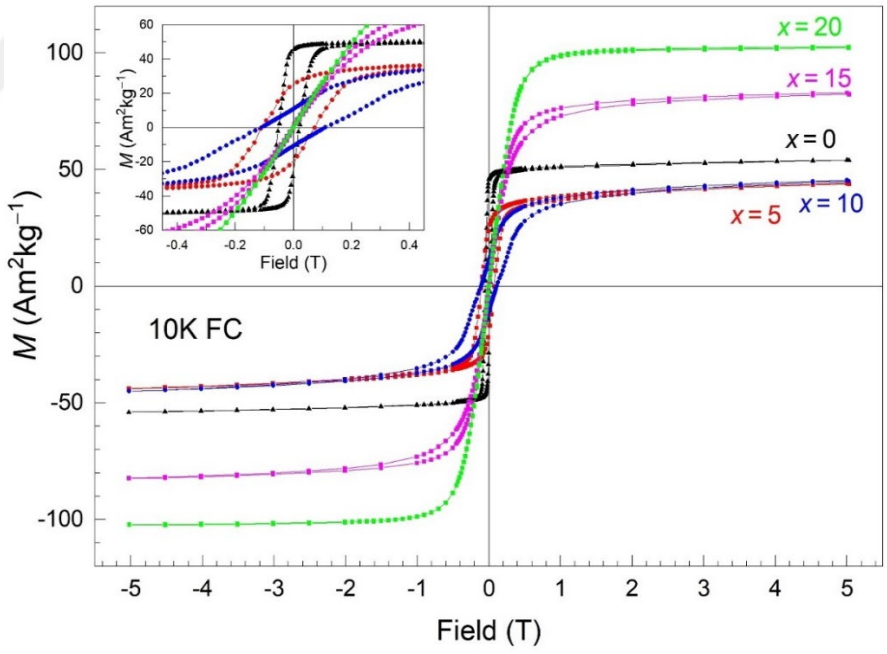

Figure 4.7. Field-dependent magnetization measurements of $(MnFeCoNi)_{80}Cu_{(20-x)}Al_x$ HEAs

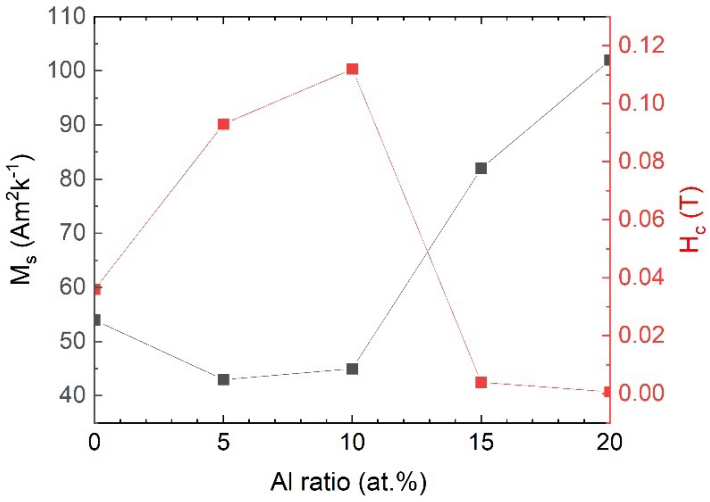

Figure 4.8. Coercive field (H_c) and saturation magnetization (M_s) as a function of x value for $(MnFeCoNi)_{80}Cu_{(20-x)}Al_x$ HEA.

Furthermore, exchange bias (EB) effects has been observed for x = 0, 5 and 10 at% samples as horizontal shifts in FC M(H) measurements as seen in Figure 4.9. The red data is obtained at 10 K in the field cooled state of the sample, while the black data shows the zero-field cooled state of same sample at 10 K. The EB effect gradually vanishes with increasing Al content. One of the effects of the exchange anisotropy achieved at the interface between an AF and an FM material is known as exchange bias (Nogués & Schuller, 1999). At the FM–AF interface, the interaction between the FM–AF spins acts to prevent the rotation of the FM spins in the direction of the applied field. When the field is sufficiently strong, the spins rotate, but rotate back easier when the field is again gradually reversed. Thus, shifts are observed at the hysteresis loops, it causes the formation of EB (Vishnoi & Kaur, 2011).

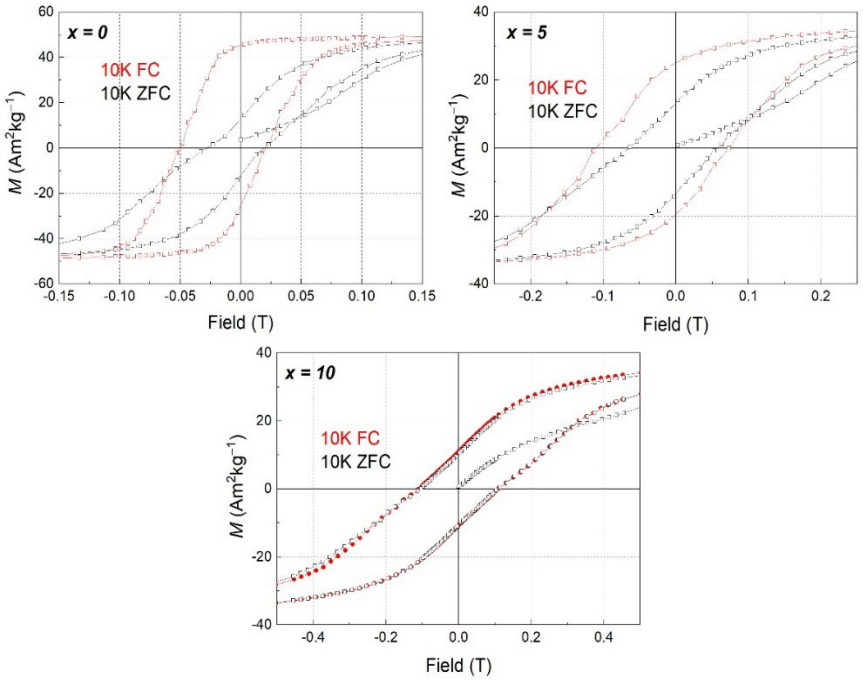

Figure 4.9. The enlarged hysteresis loops for $(MnFeCoNi)_{80}Cu_{(20-x)}Al_x$ at x=0, 5 and 10 at%.

Additionally, due to same reason as the EB effect, double-shifted hysteresis loop has been observed during ZFC especially with the x=0 sample in Figure 4.9. This double-shifted hysteresis loop consists of two sub-loops shifting in different directions such as one subloop shifts into the positive field while the other shifting into the negative field. It can be understood in this study that when the Al concentration increases, the FM interaction takes charge, and the AF anisotropy decreases. Thus, the EB eff ect diminishes.

4.1.4. Micro-hardness measurements

The minimum, maximum and average values of the measured microhardness of each alloy for the $(MnFeCoNi)_{80}Cu_{(20-x)}Al_x$ HEAs are given in Table 4.4. Considering the hardness results in relation to the Al content, an increase was observed with increasing Al content and the resulting BCC phase formation in the microstructure. For the alloys with x = 15 and 20 at% with the highest phase fractions of BCC, the micro-hardness values are the highest. The BCC phase is substantially stronger than the FCC phase. The reason for this is thought to be because of the increase in the elastic modulus by

the presence of elements such as Al with strong binding characteristics in the BCC phase (J. M. Wu et al., 2006).

Table 4.4. The micro-hardness variation of $(MnFeCoNi)_{80}Cu_{(20-x)}Al_x$ alloys.

Al (at%)	Min. HV	Max. HV	Avr. HV
x=0	186.6	199.8	194.1
x=5	187.6	215.2	201.1
x=10	197.3	207.0	202.4
x=15	399.9	434.1	420.0
x=20	477.9	507.8	494.8

4.2. $Mn_{20}Fe_{20}Co_{20}Ni_{20}Cu_{(20-x)}Ga_x$ High Entropy Alloy

In this section, XRD, EDX, magnetization and hardness results of $(MnFeCoNi)_{80}Cu_{(20-x)}Ga_x$ HEAs with x = 0, 5, 10, 15 and 20 at% are discussed.

4.2.1. XRD measurements

XRD results for $(MnFeCoNi)_{80}Cu_{(20-x)}Ga_x$ HEAs with x = 0, 5, 10, 15 and 20 at% are given in Figure 4.10. The base $(MnFeCoNi)_{80}Cu_{20}$ alloy is same as the alloy is given in the previous section. Similar to the alloys with Al, for HEAs with Ga, an FCC - BCC phase transition was observed as the Ga content increased. The first BCC formation was detected for x = 15 at%. Compared to the Al series, the BCC phase formation starts at higher Ga addition. In contrast to HEAs with Al, in this case the formation of the B2 structure was not observed in XRD data.

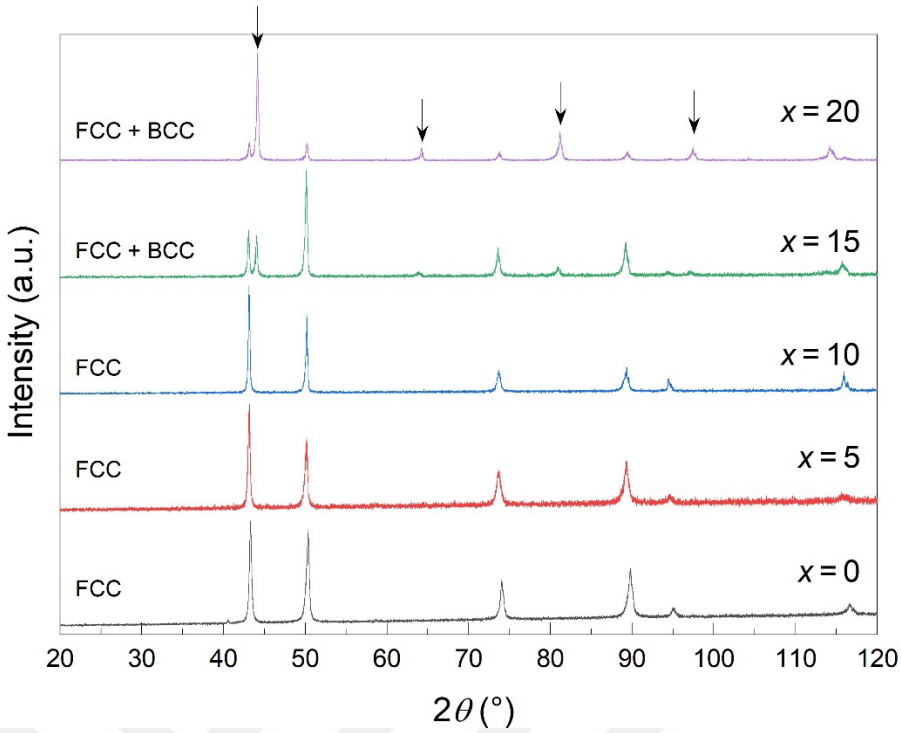

Figure 4.10 XRD data of $(MnFeCoNi)_{80}Cu_{(20-x)}Ga_x$ alloys

Figure 4.11a-e show Rietveld-refined XRD pattern profiles of the alloys. The Fm-3m space group was used for the FCC structure, and the BCC structure was refined with the Im-3m space group. In Figure 4.11a-e, black and red data correspond to calculated and measured data, respectively. The difference between the observed and calculated data is represented by blue lines. Bragg peak positions of the phases are represented by black bars. The pure FCC structure is fitted for the alloys with x = 0, 5 and 10 at%, while the BCC structure contributes to the refinement for x = 15 and 20 at% alloys.

The lattice parameters and phase fractions obtained from the refinements are given in Table 4.5. The lattice parameters of the FCC phase first increase with the addition of Ga atom having a larger atomic radius than the other atoms. Then it remains almost constant for the other alloys. The lattice parameter of the BCC structure also remains constant with varying Ga content, and it is the same with that of obtained the alloys with Al. The phase fractions of the FCC and BCC phases for x = 15 and 20 at% are almost inverted according to Table 4.5. The 22% of BCC for x = 15 at% increases to 79% with 5% of Ga addition.

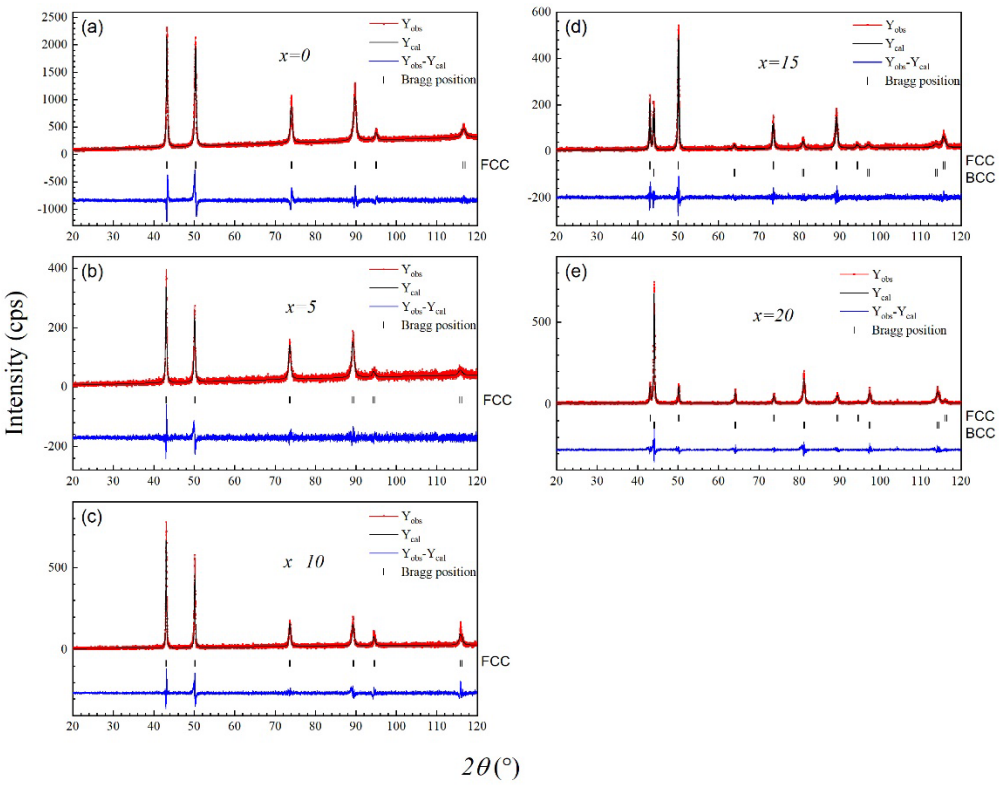

Figure 4.11 Rietveld refinement XRD data of $(MnFeCoNi)_{80}Cu_{(20-x)}Ga_x$ alloys (a) x = 0, (b) x=5, (c) x=10 (d) x=15 and (e) x=20 at%

Table 4.5. Lattice parameters and phase fractions $(MnFeCoNi)_{80}Cu_{(20-x)}Ga_x$ HEAs.

Ga (at%)	Lattice Parameters		Phase Fractions	
	fcc (Å)	bcc (Å)	fcc	bcc
x=0	3.6201	-	1	-
x=5	3.6402	-	1	-
x=10	3.6382	-	1	-
x=15	3.6407	2.9099	0.78	0.22
x=20	3.6348	2.9022	0.21	0.79

4.2.2. EDX analysis

EDX mapping and point analysis were performed to obtain the chemical compositions of the phases and element distributions in $(MnFeCoNi)_{80}Cu_{(20-x)}Ga_x$ high entropy alloys. The mapping results for all elements are given in Figure 4.12a-e for x = 0, 5,

10, 15 and 20 at% alloys, respectively. The scale bar given in the electron images corresponds to 50 μm. Figures 4.12a-c show the homogenous distribution of the elements for x = 0, 5 and 10 at% alloys and correlate with XRD results as observed single FCC phase. The regions of two different phases seen as a darker and a brighter contrast were observed for the sample x=15 and 20 at% (Figure 4.12d and e). For these two samples, the FCC phase has a larger region because the phase fraction of the FCC phase is larger than the BCC phase as obtained from refinement results. In this case, the brighter regions for Ni and Ga elements represent the BCC phase while the brighter region for Fe corresponds to the FCC phase. At x=20 (Figure 4.12e), it is seen that the regions corresponding to the BCC phase has increased in size and constitutes the main phase of the alloy.

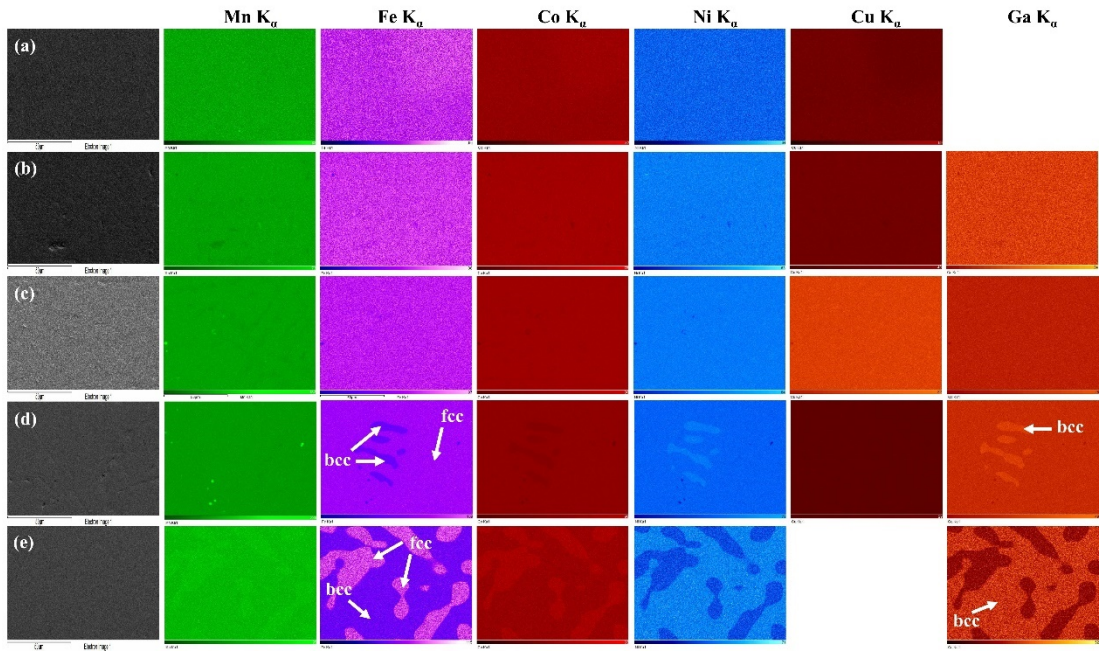

Figure 4.12. EDX elemental mapping results of $(MnFeCoNi)_{80}Cu_{(20-x)}Ga_x$ HEAs, (a) x=0, (b) x=5, (c) x=10, (d) x=15 and (e) x=20 at%.

The chemical compositions and e/a values of $(MnFeCoNi)_{80}Cu_{(20-x)}Ga_x$ HEAs are given in Table 4.6. For x = 0, 5, and 10 at%, the compositions of the homogeneously distributed single FCC phase were obtained. For x = 15 and 20 at% alloys, the composition of both FCC and BCC phases were acquired as given in Table 4.6. The

addition of Ga promotes the formation of the BCC phase. We can also conclude that Ga and Ni prone to be in the BCC phase, while the FCC is enriched with Fe.

As shown in Table 4.6, when the Ga concentration increases, the e/a values decrease and form the BCC phase. As it also seen in the Al added HEAs, the single FCC phase becomes stable and forms for e/a ≥ 8, while both BCC and FCC phases are stable in between 6.87 < e/a < 8.0.

Table 4.6 Chemical compositions and e/a values for $(MnFeCoNi)_{80}Cu_{(20-x)}Ga_x$ HEAs.

Ga (at%)	FCC		BCC	
	Chemical Composition	e/a	Chemical Composition	e/a
x=0	$Mn_{18.2}Fe_{21.0}Co_{21.0}Ni_{20.5}Cu_{19.3}$	9.02	--	-
x=5	$Mn_{16.5}Fe_{22.2}Co_{21.6}Ni_{19.7}Cu_{12.8}Ga_{7.2}$	8.47	--	-
x=10	$Mn_{17.6}Fe_{23.2}Co_{22.1}Ni_{19.2}Cu_{8.1}Ga_{9.7}$	8.18	--	-
x=15	$Mn_{18.4}Fe_{22.4}Co_{21.7}Ni_{19.0}Cu_{4.3}Ga_{14.2}$	7.83	$Mn_{18.1}Fe_{14.3}Co_{17.6}Ni_{23.7}Cu_{5.2}Ga_{21.1}$	7.57
x=20	$Mn_{19.0}Fe_{29.2}Co_{21.7}Ni_{15.6}Ga_{14.4}$	7.61	$Mn_{19.0}Fe_{18.8}Co_{19.8}Ni_{21.1}Ga_{21.3}$	7.37

4.2.3. Magnetization measurements

M(T) measurements under 5 mT and 5 T external magnetic fields and M(H) measurements performed for $(MnFeCoNi)_{80}Cu_{(20-x)}Ga_x$ HEAs are given in Figure 4.13a-e. The M(T) measurements were performed in the temperature range of 10 K ≤ T ≤ 380 K under 5 mT and 5 T external magnetic fields using a SQUID magnetometer. M(T) measurements were also carried out at high temperatures between 380 K ≤ T ≤ 780 K under a 5 mT external magnetic field for the alloys with x = 0, 15 and 20 at%.

The low temperature measurements are given with blue lines and the high temperature measurements are represented by red lines. The splitting between ZFC and FC susceptibilities is also observed below T_c for the samples with x = 0, 5 and 10 at% Ga. It is seen that the splitting decreases with increasing Ga concentration and disappears for the x = 15 alloy. It is understood that while the alloys initially exhibit coexistence

of FM and AF interactions, it begins to show completely FM characteristics as the Ga content increases.

The T_c and M_s values for each phase of the alloys are given in Table 4.7. The T_c of the FCC phase decreases with increasing Ga content for the alloys with x = 0, 5 and 10 at% (Figure 4.13a-c). Then, the T_c of the FCC phase only remains as a cusp around 85 K for x = 15 and 20 at% (Figure 4.13d and e). This shows that the AF behavior remains from the FM-AF mixed state of the FCC structure. The second T_c appears at high temperatures for x = 15 and 20 at% alloys with the formation of the BCC phase (Figure 4.13d and e). T_c corresponding to the BCC phase also increases with increasing Ga content for these two alloys, in contrast to $(MnFeCoNi)_{80}Al_{20}$ alloy with a decreasing T_c as a result of the formation of ordered B2 structure.

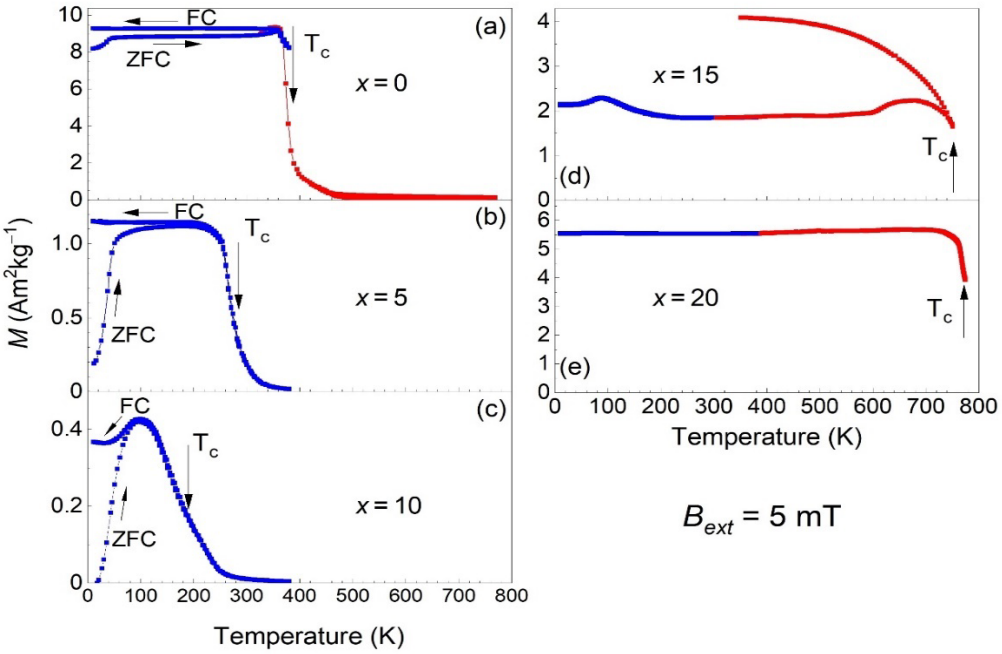

Figure 4.13 Temperature-dependent magnetization curves under 5 mT external magnetic field for $(MnFeCoNi)_{80}Cu_{(20-x)}Ga_x$ with x = 0, 5, 10, 15 and 20 at% represented in (a), (b), (c), (d) and (e) respectively.

Figure 4.14 shows the M(T) measurements carried out under 5 T external magnetic field. From these measurements, the M_s values are determined and given in Table 4.7. A slight decrease in M_s value was observed with the addition of Ga into the equimolar $Mn_{20}Fe_{20}Co_{20}Ni_{20}Cu_{20}$ HEA. However, it increases with further Ga amount and results in BCC formation. For x = 20 at%, the highest value of M_s was found as 98 Am^2/kg.

In this context, it is obvious that one of the contributing factors to obtain high saturation magnetization is the formation of the BCC phase.

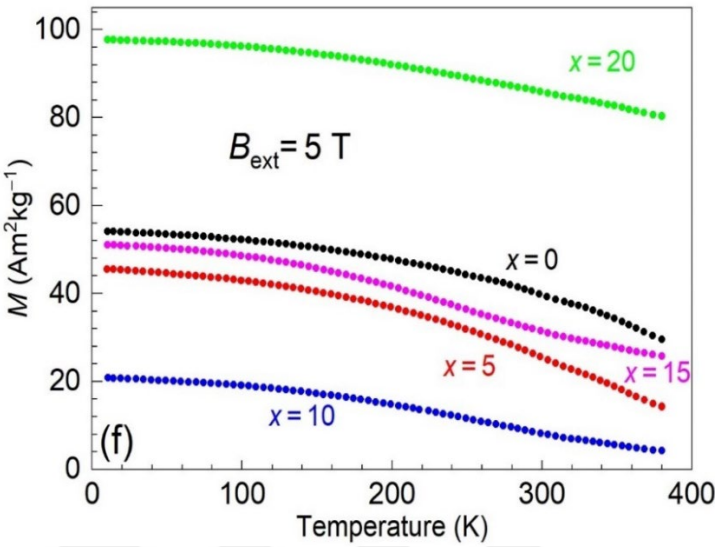

Figure 4.14 Temperature dependent magnetization measurements for $(MnFeCoNi)_{80}Cu_{(20-x)}Ga_x$ HEAs under 5 T external field.

Table 4.7. Saturation magnetization (M_s) and Curie temperature (T_c) of $(MnFeCoNi)_{80}Cu_{(20-x)}Ga_x$ HEAs.

Ga at%	M_s (Am^2/kg)	T_c (K)	
		FCC	BCC
x=0	54	374	-
x=5	46	266	-
x=10	21	151	-
x=15	51	85 (T_N)	750
x=20	98	-	772

Figure 4.15 shows the M(H) measurements of $(MnFeCoNi)_{80}Cu_{(20-x)}Ga_x$ HEAs. The coercive fields obtained from the hysteresis loops H_c are shown in Figure 4.16 with M_s values together. The $(MnFeCoNi)_{80}Cu_{(20-x)}Ga_x$ HEAs exhibit soft ferromagnetic behavior with increasing amount of Ga or with the formation the BCC phase similar to the Al-series samples. The initial mixed FM-AF interactions coming from the FCC

feature diminishes, and soft magnetic interactions become dominant. For this reason, as seen in Figure 4.16, H_c decreases while the M_s increases in hysteresis loops.

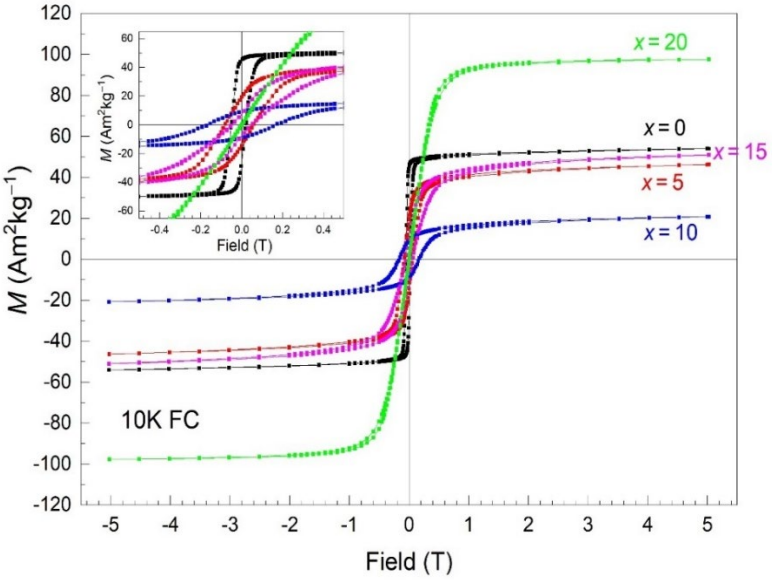

Figure 4.15. M(H) measurement results for $(MnFeCoNi)_{80}Cu_{(20-x)}Ga_x$ HEAs.

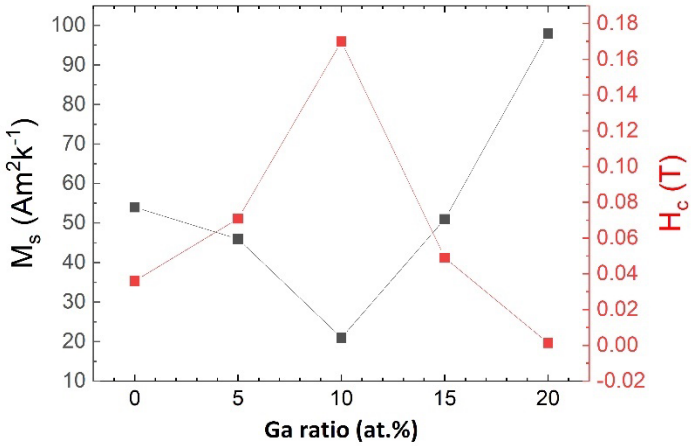

Figure 4.16. Coercivity (H_c) and saturation magnetization (M_s) as a function of x for $(MnFeCoNi)_{80}Cu_{(20-x)}Ga_x$ HEAs.

As a result of the mixed FM-AF interactions of the FCC phase, in low field M(T) measurements, we observed a splitting between ZFC and FC measurements. This also gives rise to a horizontal shift in hysteresis loops measured at 10 K for the field-cooled state. The horizontal shift and resulting EB effect observed in $(MnFeCoNi)_{80}Cu_{20}$

alloy in the previous section also remains with the addition of small amount of Ga for x = 5 at% and disappears for x = 10 at%, as given Figure 4.18.

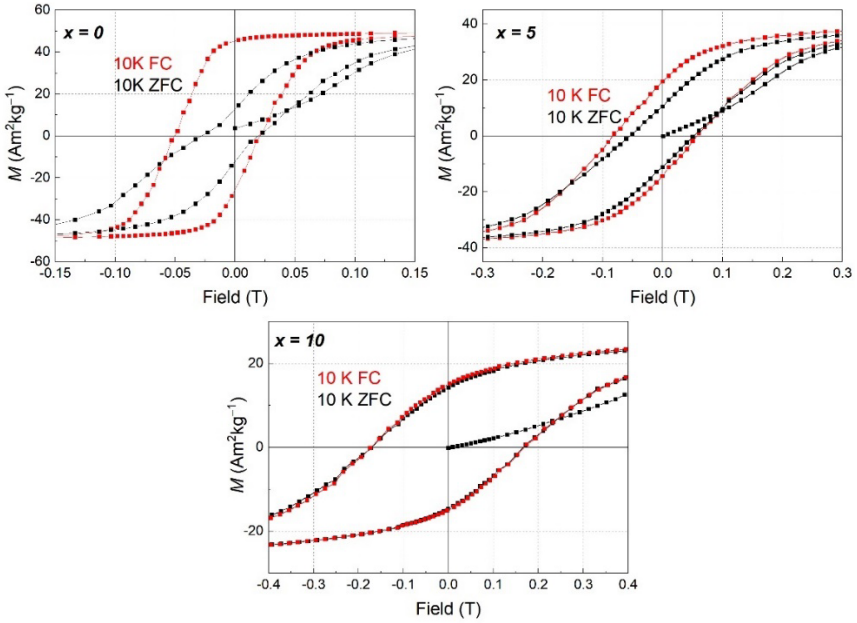

Figure 4.167. The enlarged hysteresis loops for $(MnFeCoNi)_{80}Cu_{(20-x)}Ga_x$ for x = 0, 5 and 10 at%.

4.2.4. Micro-hardness measurements

Table 4.8 shows the minimum, maximum, and average micro-hardness values of each sample for the $(MnFeCoNi)_{80}Cu_{(20-x)}Ga_x$ HEAs. It is seen that the obtained results are similar to those of the Al series. Likewise, the increase in the Ga concentration in the alloy gives rise to an increase of hardness values. This is due to the formation of the BCC.

Table 4.8. The micro-hardness variation of $(MnFeCoNi)_{80}Cu_{(20-x)}Ga_x$ alloys.

Ga (at%)	Min. HV	Max. HV	Avr. HV
x=0	186.6	199.8	194.1
x=5	196.1	216.9	203.8
x=10	189.7	226.1	215.1
x=15	262.3	288.6	275.0
x=20	490.0	554.4	518.2

4.3. Magnetocaloric Effect for $(MnFeCoNi)_{80}Cu_{20}$

The magnetocaloric effect (MCE) manifests itself in all magnetic materials. This effect is based on the fact that the material absorbs or dissipate heat when an external magnetic field is applied or removed. When a magnetic field is applied, the magnetic entropy value decreases, and heat is isothermally transferred from the magnetic cooling system to the environment. Conversely, when the magnetic field is removed, the magnetic entropy increases, and the heat is dissipated from the system, and it is absorbed adiabatically (Akdemir et al., 2014).

A material that exhibits the magnetocaloric effect tends to release heat when a magnetic field is applied because its magnetic moments align parallel to the applied magnetic field and to conserve the entropy, the amplitude of lattice vibrations increases. The material tends to cool down when a magnetic field is removed because the alignment of the magnetic moments is reverted back to initial more random state, while the amplitude of lattice vibrations decreases. The MCE can also be observed in magnetic material around T_c.

In this study, the magnetocaloric properties of $(MnFeCoNi)_{80}Cu_{20}$ (x = 0) were investigated. In order to determine the entropy changes of the alloy, firstly isothermal magnetization curves were measured in 5 K steps in the temperature range 350 - 385 K which is around T_c as given in Figure 4.18.

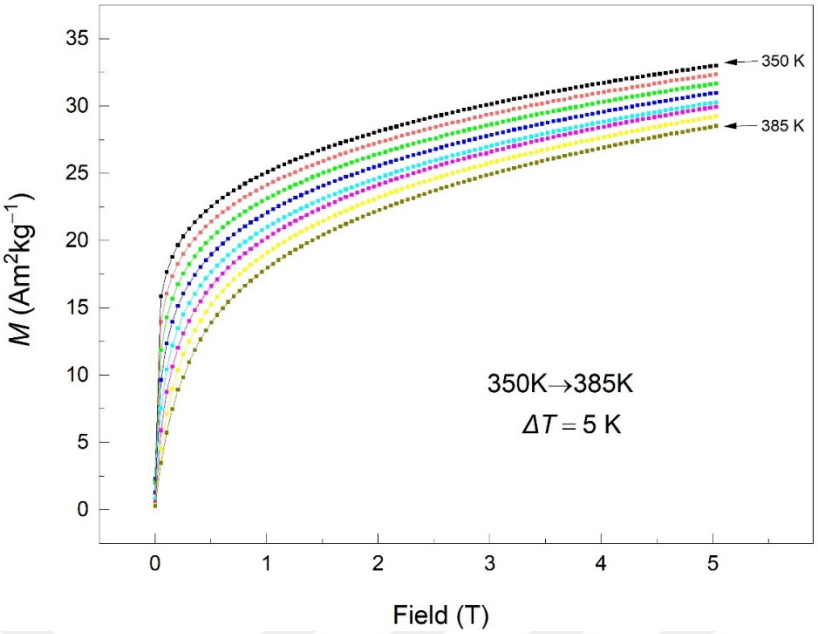

Figure 4.18. The magnetization isotherms for $(MnFeCoNi)_{80}Cu_{20}$ HEA.

The entropy change ΔS with respect to H is given by the Maxwell relationship:

$$\left(\frac{\partial S}{\partial H}\right)_T = \left(\frac{\partial M}{\partial T}\right)_H. \tag{4.1}$$

This can be expressed in the integral form:

$$\Delta S = \int_{H1}^{H2} \left(\frac{\partial M}{\partial T}\right)_H dH, \tag{4.2}$$

And can be integrated numerically using:

$$\Delta S = \sum_i \frac{M_i - M_{i+1}}{T_i - T_{i-1}} \Delta H \tag{4.3}$$

The temperature dependence of ΔS for $(MnFeCoNi)_{80}Cu_{20}$ HEA are shown in Figure 4.19. The value of isothermal magnetic entropy change (ΔS_M) slowly increased with increasing temperature, then suddenly decreased where the temperature approaches T_c of 373 K) and then increased again.

The entropy change taking place around the Curie temperature increases with increasing magnetic field and remains non-zero outside the range of T_c.

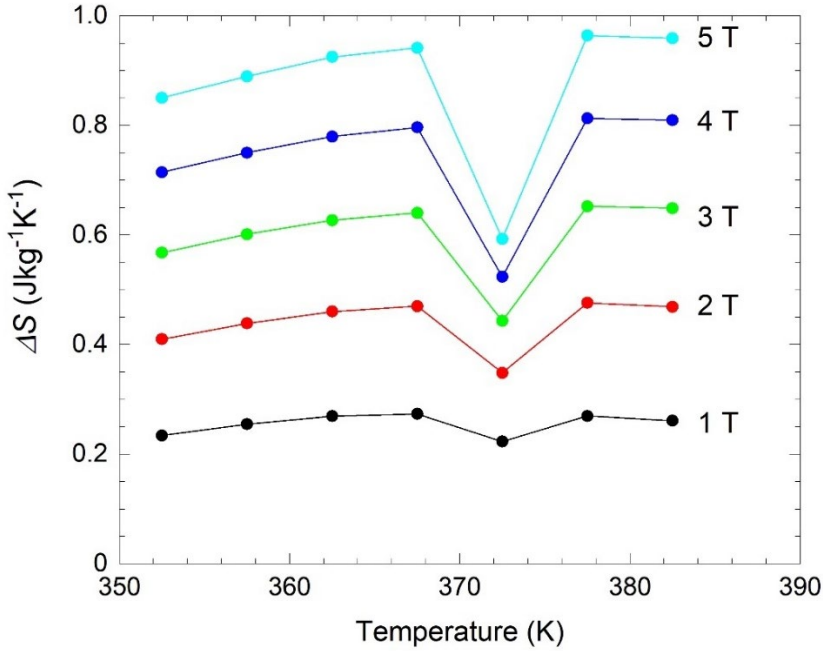

Figure 4.179. Temperature dependent magnetic entropy change of $(MnFeCoNi)_{80}Cu_{20}$ HEA.

5. CONCLUSION

In this thesis, $(MnFeCoNi)_{80}Cu_{(20-x)}Al_x$ and $(MnFeCoNi)_{80}Cu_{(20-x)}Ga_x$ HEAs with x = 0, 5, 10, 15 and 20 at % were produced by vacuum arc-melting method. Both alloy series were examined in terms of the crystal structures, magnetization, and hardness using X-ray diffraction (XRD), energy dispersive x-ray analysis (EDX), superconducting quantum interference device (SQUID) magnetometery and a Vickers micro-harness device. The conclusions and findings of the study are summed up as in the subsections given below.

$(MnFeCoNi)_{80}Cu_{(20-x)}Al_x$ HEAs with x = 0, 5, 10, 15 and 20 at %,

i. According to XRD and EDX results, the base sample with x=0 exhibits single FCC crystal structure. The addition of Al element promotes the formation of the BCC phase by varying compositions of two phases. While Al and Ni have been enriched in the BCC phase, Fe mostly prefers to remain in the FCC structure. Additionally, the $(MnFeCoNi)_{80}Al_{20}$ alloy was found to possesses the B2 phase as an ordered intermetallic.

ii. According to the magnetization results, M(T) performed under a low (5 mT) external magnetic field shows that there are two distinct T_cs belong to the FCC and the BCC phases. The FCC phase exhibits FM-AF mixed magnetic interactions while the BCC phase forms with its pure ferromagnetic behavior. The T_c of the FCC phase decreases with increasing amount of Al and only the AF part of FCC phase remains for the alloy with x = 15 at%. It is found that the T_c of the BCC phase occurs at very high temperatures and increases with increasing amount of Al for x = 10 and 15 at%. For x = 20 at% of Al, the T_c decreases slightly and this can be attributed to the formation of the ordered B2 structure. Moreover, the splitting between ZFC and FC susceptibility was observed in alloys showing FM-AF mixed interactions. The M(T) measurements performed under a high (5 T) external magnetic field showed that M_s values were found as a 54, 43, 45, 82 and 102 Am^2/kg, for x = 0, 5, 10, 15 and 20, respectively. It was found that the x=20 at% alloy exhibits BCC/B2 and FCC phases together and possesses the highest M_s value. From M(H) results, the H_c values are obtained and correlated with the

variation of M_s and Al content. The results show that with increasing amount of Al, the hysteresis loops become narrower with increasing M_s and decreasing H_c. The alloys exhibit soft magnetic behavior and dominate over the AF behavior for high Al contents.

iii. According to the hardness results, for alloys with the FCC crystal structure, there has been no noticeable changes in micro-hardness. However, the formation of BCC phase increases the hardness values significantly. The hardness value of the alloys, which was initially 194.1 HV for single FCC phase, increased to 494.8 HV for duplex FCC-BCC phase with the addition of Al.

For $Mn_{20}Fe_{20}Co_{20}Ni_{20}Cu_{(20-x)}Ga_x$ HEAs with x = 0, 5, 10, 15 and 20 at %,

i. The crystal structure of $Mn_{20}Fe_{20}Co_{20}Ni_{20}Cu_{(20-x)}Ga_x$ HEAs are also affected by changing Cu and Ga concentrations. It is evidenced that, x = 0, 5 and 10 at% alloys are formed homogeneously in the FCC structure by elemental mapping analysis. For x = 15 at%, the BCC phase is detected in addition to the FCC. The Ga element favors the formation of the BCC phase in HEAs because it is found that the phase fraction of the BCC phase increases with the addition of Ga for x = 20 at%. Similarly, the BCC phase is prone to be enriched with Ni and Ga, while the FCC phase is formed with a high amount of Fe element.

ii. As a result of the M(T) measurements performed under 5 mT external magnetic field, we obtained similar T_c values for both FCC and BCC phases. As mentioned for the Al series, the BCC phase exhibits T_c at high temperatures, while the T_c of the FCC phase decreases with increasing amount of Ga. Splitting between ZFC and FC was also observed for x = 0, 5 and 10 at% alloys due to the presence of FM-AF mixed magnetic interactions. M_s values are found from 5 T M(T) measurements, and H_c values are obtained from M(H) measurements. M_s increases and H_c decreases with the formation of the BCC phase giving rise to pure ferromagnetic behavior in these alloys.

iii. The hardness value of the samples with a single FCC phase which are x=0, 5 and 10 are found as 194.1, 203.8 and 215.1 HV, respectively. After formation of the BCC phase, the hardness values of the alloys with x=15 and 20 at% increases as 275.0 and 518.2 HV due to the strong bonding nature of the BCC phase.

We have also investigated the MCE for $(MnFeCoNi)_{80}Cu_{20}$ alloy by calculating the entropy change ΔS from the first quadrant of M(H) measurements taken around T_c. The maximum entropy change was found as 0.96 $Jkg^{-1}K^{-1}$ around T_c at 5 T magnetic field. The entropy change does not reduce to zero in the measured temperature range. This can be interpreted that a small amount of heat exchange and entropy change around 0.2 $Jkg^{-1}K^{-1}$ can always be stored in HEAs. However, this needs to be verified with some additional measurements.

We calculated the average magnetic moment values by using the lattice parameters, phase fractions, e/a and M_s values. The average magnetic moment values are interpreted as a function of e/a and Slater-Pauling rule. The Slater-Pauling rule shows how the magnetic moment of 3d-transition metals varies with e/a (Pauling, 1938; Slater J. C. 1936). The data obtained in this study are plotted in Figure 5.1 and given in Table 5.1 for each phase. In the Slater-Pauling curve given in Figure 5.1, the red and purple stars correspond to the values of the Al alloy series for FCC and BCC phases, respectively. Additionally, blue empty circles and purple triangles shows the values for the Ga alloy series for FCC and BCC phases, respectively. According to the e/a for both alloy series, the FCC phase is stabilized in the range of $7.61 \leq e/a \leq 9.02$, while BCC phase is stabilized in the range of $7.37 \leq e/a \leq 7.96$. The addition of Al and Ga decreased the e/a value while leading to an increase in the average magnetic moment. In terms of Slater-Pauling rule, the HEAs studied in this work obey this rule as Heusler alloys. The values are well fitted at the region for that for Heusler alloys.

Table 5.1. Average magnetic moment as a function of x for $(MnFeCoNi)_{80}Cu_{(20-x)}Al_x$ and $(MnFeCoNi)_{80}Cu_{(20-x)}Ga_x$ HEAs.

Al (at%)	Average moment (μ_B)		Ga (at%)	Average moment (μ_B)	
	FCC	BCC		FCC	BCC
x = 0	0.57	--	x = 0	0.57	--
x = 5	0.46	--	x = 5	0.46	--
x = 10	0.75	0.09	x = 10	0.75	0.09
x = 15	1.20	0.58	x = 15	1.20	0.58
x = 20	1.26	0.82	x = 20	1.26	0.82

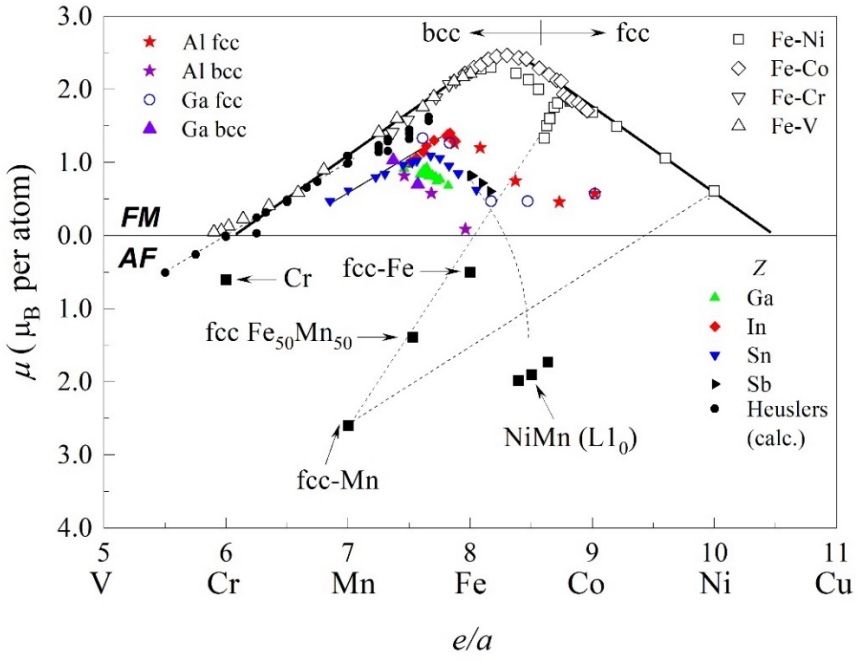

Figure 5.1. Slater-Pauling curve. The points from this study are ★ refers to FCC in Al series, ★ refers to BCC in Al series, ○ refers to FCC in Ga series and ▲ refers to BCC in Ga series

REFERENCES

Akdemir, M., Ekren, O., & Yılancı, A. (2014). Manyetokalorik Malzemeler ve Manyetik Soğutmanın Temelleri. *Ttmd*.

Başkut, S., & Turan, S. (2022). Kaplama Malzemelerin Taramalı Elektron Mikroskobunda Tahribatsız Kimyasal Analizleri. *Düzce Üniversitesi Bilim ve Teknoloji Dergisi*, *10*, 448–464. https://doi.org/10.29130/dubited.950588

Bragg, W. H. and W. L. Bragg. (1913) "The Reflection of X-Rays by Crystals." Proceedings of the Royal Society of London. Series A, Containing Papers of a Mathematical and Physical Character 88(605):428–38.

Cantor, B., Chang, I. T. H., Knight, P., & Vincent, A. J. B. (2004). Microstructural development in equiatomic multicomponent alloys. *Materials Science and Engineering A*, *375–377*(1-2 SPEC. ISS.), 213–218. https://doi.org/10.1016/j.msea.2003.10.257

Chen, Y. Y., Duval, T., Hung, U. D., Yeh, J. W., & Shih, H. C. (2005). Microstructure and electrochemical properties of high entropy alloys-a comparison with type-304 stainless steel. *Corrosion Science*, *47*(9), 2257–2279. https://doi.org/10.1016/J.CORSCI.2004.11.008

Chuang, M. H., Tsai, M. H., Wang, W. R., Lin, S. J., & Yeh, J. W. (2011). Microstructure and wear behavior of AlxCo 1.5CrFeNi1.5Tiy high-entropy alloys. *Acta Materialia*, *59*(16), 6308–6317. https://doi.org/10.1016/j.actamat.2011.06.041

Coey, J. M. D. (2010). Magnetism and Magnetic Materials. In *Cambridge University Press*. https://www.researchgate.net/publication/269107473_What_is_governance/link/548173090cf22525dcb61443/download%0Ahttp://www.econ.upf.edu/~reynal/Civil wars_12December2010.pdf%0Ahttps://think-asia.org/handle/11540/8282%0Ahttps://www.jstor.org/stable/41857625

Gludovatz, B., Hohenwarter, A., Catoor, D., Chang, E. H., George, E. P., & Ritchie, R. O. (2014). A fracture-resistant high-entropy alloy for cryogenic applications. *Science*, *345*(6201), 1153–1158. https://doi.org/10.1126/science.1254581

Guo, S., Ng, C., Lu, J., & Liu, C. T. (2011). Effect of valence electron concentration on

stability of fcc or bcc phase in high entropy alloys. *Journal of Applied Physics*, *109*(10). https://doi.org/10.1063/1.3587228

Hemphill, M. A., Yuan, T., Wang, G. Y., Yeh, J. W., Tsai, C. W., Chuang, A., & Liaw, P. K. (2012). Fatigue behavior of Al 0.5CoCrCuFeNi high entropy alloys. *Acta Materialia*, *60*(16), 5723–5734. https://doi.org/10.1016/j.actamat.2012.06.046

Li, P., Wang, A., & Liu, C. T. (2017). Composition dependence of structure, physical and mechanical properties of FeCoNi(MnAl) x high entropy alloys. *Intermetallics*, *87*, 21–26. https://doi.org/10.1016/j.intermet.2017.04.007

Li, Z., Xu, H., Gu, Y., Pan, M., Yu, L., Tan, X., & Hou, X. (2018). Correlation between the magnetic properties and phase constitution of FeCoNi(CuAl)0.8Gax ($0 \leq x \leq 0.08$) high-entropy alloys. *Journal of Alloys and Compounds*, *746*, 285–291. https://doi.org/10.1016/j.jallcom.2018.02.189

Lucas, M. S., Mauger, L., Muoz, J. A., Xiao, Y., Sheets, A. O., Semiatin, S. L., Horwath, J., & Turgut, Z. (2011). Magnetic and vibrational properties of high-entropy alloys. *Journal of Applied Physics*, *109*(7), 2011–2014. https://doi.org/10.1063/1.3538936

Mañosa, L., Planes, A., Acet, M., Duman, E., & Wassermann, E. F. (2003). Magnetic properties and martensitic transition in annealed Ni50Mn30Al20. *Journal of Applied Physics*, *93*(10 3), 8498–8500. https://doi.org/10.1063/1.1555977

Mishra, R. K., & Shahi, R. R. (2018). Magnetic Characteristics of High Entropy Alloys. *Magnetism and Magnetic Materials*. https://doi.org/10.5772/intechopen.74235

Murty, B. S., Yeh, J. W., Ranganathan, S., & Bhattacharjee, P. P. (2019). High-entropy alloys. In *Elsevier* (Second). Elsevier. https://doi.org/https://doi.org/10.1016/C2017-0-03317-7

Na, S.-M., Yoo, J.-H., Lambert, P. K., & Jones, N. J. (2018). Room-temperature ferromagnetic transitions and the temperature dependence of magnetic behaviors in FeCoNiCr-based high-entropy alloys. *AIP ADVANCES*, *8*. https://doi.org/10.1063/1.5007073

Nogués, J., & Schuller, I. K. (1999). Exchange bias. *Journal of Magnetism and Magnetic Materials*, *192*(2), 203–232. https://doi.org/10.1016/S0304-8853(98)00266-2

Otto, F., Yang, Y., Bei, H., & George, E. P. (2013). Relative effects of enthalpy and entropy on the phase stability of equiatomic high-entropy alloys. *Acta Materialia*, *61*(7), 2628–2638. https://doi.org/10.1016/j.actamat.2013.01.042

Pauling, L. (1938). The nature of the interatomic forces in metals. Physical Review, 54(11), 899–904

Petricek, M.D.V. and L. Palatinus, (2014) Jana2006, Z. Krist. 229:345-352.

Pu, Y., Zhang, Q., Li, R., Chen, M., Du, X., & Zhou, S. (2019). Dielectric properties and electrocaloric effect of high-entropy (Na0.2Bi0.2Ba0.2Sr0.2Ca0.2)TiO3 ceramic. *Applied Physics Letters*, *115*(22), 0–5. https://doi.org/10.1063/1.5126652

Ranganathan, S. (2003). Alloyed pleasures: Multimetallic cocktails. *Current Science*, *85*(10), 1404–1406. https://doi.org/10.2307/24108817

Rao, Z., Dutta, B., Körmann, F., Ponge, D., Li, L., He, J., Stephenson, L., Schäfer, L., Skokov, K., Gutfleisch, O., Raabe, D., & Li, Z. (2020). Unveiling the mechanism of abnormal magnetic behavior of FeNiCoMnCu high-entropy alloys through a joint experimental-theoretical study. *Physical Review Materials*, *4*(1). https://doi.org/10.1103/PhysRevMaterials.4.014402

Saito, T., Furuta, T., Hwang, J. H., Kuramoto, S., Nishino, K., Suzuki, N., Chen, R., Yamada, A., Ito, K., Seno, Y., Nonaka, T., Ikehata, H., Nagasako, N., Iwamoto, C., Ikuhara, Y., & Sakuma, T. (2003) Multifunctional alloys obtained via a dislocation-free plastic deformation mechanism, Science, 300(5618): 464–467. https://doi.org/10.1126/science.1081957

Senkov, O. N., Senkova, S. V., & Woodward, C. (2014). Effect of aluminum on the microstructure and properties of two refractory high-entropy alloys. *Acta Materialia*, *68*, 214–228. https://doi.org/10.1016/j.actamat.2014.01.029

Slater J. C. 1936. “The Ferromagnetism of Nickel.” Physical Review 44(10):850–53.

Srivatsan, T. S., & Gupta, M. (2020). High Entropy Alloys: Innovations, Advances, and Applications. In *Angewandte Chemie International Edition, 6(11), 951–952.* (1st editio). CRC Press.

Tong, C. J., Chen, M. R., Chen, S. K., Yeh, J. W., Shun, T. T., Lin, S. J., & Chang, S. Y. (2005). Mechanical performance of the AlxCoCrCuFeNi high-entropy alloy system with multiprincipal elements. *Metallurgical and Materials Transactions A: Physical Metallurgy and Materials Science*, *36*(5), 1263–1271. https://doi.org/10.1007/s11661-005-0218-9

Tsai, K. Y., Tsai, M. H., & Yeh, J. W. (2013). Sluggish diffusion in Co-Cr-Fe-Mn-Ni high-entropy alloys. *Acta Materialia*, *61*(13), 4887–4897. https://doi.org/10.1016/j.actamat.2013.04.058

Tsai, M. H. (2013). Physical properties of high entropy alloys. *Entropy*, *15*(12), 5338–5345. https://doi.org/10.3390/e15125338

Tsai, M. H., & Yeh, J. W. (2014). High-entropy alloys: A critical review. *Materials Research Letters*, *2*(3), 107–123. https://doi.org/10.1080/21663831.2014.912690

Vishnoi, R., & Kaur, D. (2011). Exchange bias behaviour in magnetron sputtered Ni49.8Mn 36.1Sn13.9 ferromagnetic shape memory alloy thin film. *Journal of Alloys and Compounds*, *509*(6), 2833–2837. https://doi.org/10.1016/J.JALLCOM.2010.11.133

Wang, W. R., Wang, W. L., & Yeh, J. W. (2014). Phases, microstructure and mechanical properties of AlxCoCrFeNi high-entropy alloys at elevated temperatures. *Journal of Alloys and Compounds*, *589*, 143–152. https://doi.org/10.1016/j.jallcom.2013.11.084

Wu, J. M., Lin, S. J., Yeh, J. W., Chen, S. K., Huang, Y. S., & Chen, H. C. (2006). Adhesive wear behavior of AlxCoCrCuFeNi high-entropy alloys as a function of aluminum content. *Wear*, *261*(5–6), 513–519. https://doi.org/10.1016/j.wear.2005.12.008

Wu, Z., Li, B., Chen, M., Yang, Y., Zheng, R., Yuan, L., Li, Z., Tan, X., & Xu, H. (2022). Tailoring magnetic property and corrosion resistance of FeCoNiCuAl high-entropy alloy with Ce additive. *Journal of Alloys and Compounds*, *901*. https://doi.org/10.1016/J.JALLCOM.2022.163665

Xu, J., Shang, C., Ge, W., Jia, H., Liaw, P. K., & Wang, Y. (2016). Effects of elemental addition on the microstructure, thermal stability, and magnetic properties of the mechanically alloyed FeSiBAlNi high entropy alloys. *Advanced Powder*

Technology, *27*(4), 1418–1426. https://doi.org/10.1016/J.APT.2016.04.037

Yeh, J. W. (2006). Recent progress in high-entropy alloys. *Annales de Chimie: Science Des Materiaux*, *31*(6), 633–648. https://doi.org/10.3166/acsm.31.633-648

Yeh, J. W. (2013). Alloy design strategies and future trends in high-entropy alloys. *Jom*, *65*(12), 1759–1771. https://doi.org/10.1007/s11837-013-0761-6

Yeh, J. W., Chen, S. K., Lin, S. J., Gan, J. Y., Chin, T. S., Shun, T. T., Tsau, C. H., & Chang, S. Y. (2004). Nanostructured high-entropy alloys with multiple principal elements: Novel alloy design concepts and outcomes. *Advanced Engineering Materials*, *6*(5), 299–303. https://doi.org/10.1002/adem.200300567

Zhang, K., & Fu, Z. (2012). Effects of annealing treatment on phase composition and microstructure of CoCrFeNiTiAl x high-entropy alloys. *Intermetallics*, *22*, 24–32. https://doi.org/10.1016/j.intermet.2011.10.010

Zhang, Q., Xu, H., Tan, X. H., Hou, X. L., Wu, S. W., Tan, G. S., & Yu, L. Y. (2016). The effects of phase constitution on magnetic and mechanical properties of FeCoNi(CuAl) x (x ¼ 0e1.2) high-entropy alloys. *Journal of Alloys and Compounds*, *693*, 1061–1067. https://doi.org/10.1016/j.jallcom.2016.09.271

Zhang, Y., Zuo, T., Cheng, Y., & Liaw, P. K. (2013). High-entropy alloys with high saturation magnetization, electrical resistivity, and malleability. *Scientific Reports*, *3*, 1–7. https://doi.org/10.1038/srep01455

Zhang, Y., Zuo, T. T., Tang, Z., Gao, M. C., Dahmen, K. A., Liaw, P. K., & Lu, Z. P. (2014). Microstructures and properties of high-entropy alloys. *Progress in Materials Science*, *61*(September 2013), 1–93. https://doi.org/10.1016/j.pmatsci.2013.10.001

Zhang, Z. J., Mao, M. M., Wang, J., Gludovatz, B., Zhang, Z., Mao, S. X., George, E. P., Yu, Q., & Ritchie, R. O. (2015). Nanoscale origins of the damage tolerance of the high-entropy alloy CrMnFeCoNi. *Nature Communications*, *6*, 1–6. https://doi.org/10.1038/ncomms10143

Zuo, T., Gao, M. C., Ouyang, L., Yang, X., Cheng, Y., Feng, R., Chen, S., Liaw, P. K., Hawk, J. A., & Zhang, Y. (2017). Tailoring magnetic behavior of CoFeMnNiX (X = Al, Cr, Ga, and Sn) high entropy alloys by metal doping. *Acta Materialia*, *130*, 10–18. https://doi.org/10.1016/j.actamat.2017.03.013

Zuo, T., Zhang, M., Liaw, P. K., & Zhang, Y. (2018). Novel high entropy alloys of Fe x Co 1-x NiMnGa with excellent soft magnetic properties. *Intermetallics*, *100*, 1–8. https://doi.org/10.1016/j.intermet.2018.05.014

CURRICULUM VITAE

Personal Information

Name Surname : Y**** O****

Nationality : T.C.

Year of Birth : 1991

Gender : Male

Education

Degree	Institution/University	Graduation Year
High School	Halil Çiftçi Anatolian High School	2009
Bachelor	Muğla Sıtkı Koçman University	2016
Master (MSc.)	Muğla Sıtkı Koçman University	-

Work Experiences

Year	Place of Employment	Position
2018-2020	ŞA-RA Group A.Ş. / Adana	Quality Control Engineer
2019-2020	ŞA-RA Group A.Ş. / Ontario	Quality Control Engineer
2020-2021	Memak Steel Construction	Quality Control Chief
2021-	Muğla Sıtkı Koçman University	Research Assistant

Skills

PPAP, FMEA, APQP, Risk Analysis and Management, Machining, Additive Manufacturing, Supervision of Manufacture, Quality System Management, AutoCAD, MS Office.